

The fate of nitrogen in deep magma oceans

Ekanshu Mallick^{a,*}, Kelsey Prissel^b, Kevin Righter^c, Colin RM Jackson^a

^a *Department of Earth and Environmental Sciences, Tulane University, United States*

^b *Department of Earth, Atmospheric, and Planetary Sciences, Purdue University, United States*

^c *Department of Earth and environmental Sciences, University of Rochester, United States*

* Corresponding author at: Tulane University, 101 Blessey Hall, New Orleans, LA 70118, United States.

Email address: emallick@tulane.edu (Ekanshu Mallick)

Peer review status: This is a non-peer-reviewed preprint submitted to EarthArXiv. This manuscript has been submitted for peer-review and subsequent publication at *Geochimica et Cosmochimica Acta*. If accepted, the final version of this manuscript will be available via the ‘Peer-reviewed Publication DOI’ link on the right-hand side of this webpage.

The fate of nitrogen in deep magma oceans

Ekanshu Mallick^{a,*}, Kelsey Prissel^b, Kevin Righter^c, Colin RM Jackson^a

^a *Department of Earth and Environmental Sciences, Tulane University, United States*

^b *Department of Earth, Atmospheric, and Planetary Sciences, Purdue University, United States*

^c *Department of Earth and environmental Sciences, University of Rochester, United States*

* Corresponding author at: Tulane University, 101 Blessey Hall, New Orleans, LA 70118, United States.

Email address: emallick@tulane.edu (Ekanshu Mallick)

ABSTRACT

Nitrogen is important in planetary evolution because it is essential to life and the most abundant element in Earth's atmosphere. Here, we investigate how core formation affects the distribution of N within accreting terrestrial planets. We conducted laser-heated diamond anvil cell experiments (LH-DAC) over a wide range of high pressure-temperature-compositional (PTX) conditions (38-103 GPa, 2728-5609 K, -1.95 to -1.03 Δ IW, 0.5-3.7 NBO/T) to study nitrogen partitioning in metal-silicate systems. Combining our data with existing low and high PT results, we developed a nitrogen partitioning model applicable from early accretion to extreme PT stages associated with giant impacts. We test the robustness of our model by accurately predicting nitrogen partitioning in a multi-anvil experiment conducted independently at 15 GPa, 2573 K with oxygen fugacity of -2.5 Δ IW. Our model shows that increasing pressure, oxygen fugacity, and N concentration in the alloy make nitrogen more siderophile, while increasing temperature, oxygen and silicon contents in the alloy, and the SiO₂ content of the silicate melt make nitrogen less siderophile. Application of our model to core formation conditions under oxidized and reduced scenarios suggest that nitrogen can be siderophile or lithophile under low PT conditions but exhibits a neutral partitioning at high PT conditions (> 100 GPa, 5000 K) over a wide range of bulk planet compositions. Using our model, along with partitioning models for S and C, we examine how core formation scenarios can fractionate C/N and S/N ratios in the BSE. Our model suggests that backreaction of volatile rich cores from reduced, smaller impactors (sub-Mars-sized) within deep magma oceans can impart a wide range of C/N and S/N ratios on the magma ocean. We find that the amount of silicate entrainment has a strong control on elemental fractionations imparted to the magma oceans. Elevated C/N and S/N ratios are associated with larger degrees of silicate entrainment, and vice versa. Thus, Earth's apparent depletion of N may relate to its volatiles being reprocessed within deep magma oceans, possibly during the end stages of accretion.

Keywords: Nitrogen, Metal-silicate partitioning, Core Formation, Magma Ocean, Volatiles, LH-DAC

1. Introduction

Nitrogen, being the most abundant element in the atmosphere, plays a pivotal role in Earth's life-forming processes and is paramount in sustaining habitability on the planet. Understanding the distribution and abundance of nitrogen within the planet involves delving into its accretionary history, where planetary-scale processes like core formation and atmospheric evolution have influenced the planet's chemistry. As a volatile siderophile element (VSE), the geochemical behavior of nitrogen strongly impacts its distribution during these accretionary stages.

Earth accumulated its mass through numerous impacts that generated global or partial magma ocean (MO) environments. These MO environments facilitate reactions that set the abundance and distribution of different elements, including nitrogen within the planet (Elkins-Tanton, 2012; Tonks and Melosh, 1993; Wetherill, 1985). Magma ocean production in early accretionary stages may have been facilitated by radiogenic heating, but later stages of magma ocean production were likely driven by impacts from differentiated planetary bodies. Towards the terminal stages of its accretion, production of global and deep magma oceans were driven by giant impacts, with pressures exceeding 100 GPa and temperatures over 6000 K (Canup and Asphaug, 2001; Tonks and Melosh, 1993), and redistribute elements within global planetary reservoirs.

Magma oceans are instrumental in creating compositional differentiation across the different accretionary stages, from planetesimals to protoplanets (Davies, 1985; Halliday et al., 2001; Lee et al., 1976; Tonks and Melosh, 1993; Urey, 1955). During impacts that produce MO environments in protoplanets, the disrupted cores of the differentiated impactors smear through the MO before eventually merging with the proto-core (e.g. Dahl and Stevenson, 2010). Fluid dynamic studies show that the disrupted core emulsifies to different degrees and descends through the magma ocean while entraining different amounts of silicate mass from the magma ocean (e.g. Deguen et al., 2014). This allows for continuous backreaction of the disrupted core with the entrained silicate mass of the larger body which can redistribute elements between the MO and the reacting metal based on their relative siderophilicities. Additionally, the MO interacts with the evolving atmosphere, which terrestrial planets like Earth could acquire during their accretion. This MO-atmosphere interaction allows for the redistribution of elements between these two reservoirs based on their volatile natures, influenced by processes like magma ocean degassing and atmospheric loss, hydrodynamic outflow, non-thermal loss due to a weak or non-existent magnetosphere, and giant impact driven loss (Genda and Abe, 2003; Lammer et al., 2008; Moynier et al., 2012; Schlichting et al., 2015; Sekiya et al., 1980; Tucker and Mukhopadhyay, 2014). Consequently, the VSE behavior of nitrogen makes its abundance and distribution within a terrestrial planet susceptible to both core-MO and MO-atmosphere interactions.

Observations on the distribution of nitrogen compared to other VSEs (H, C, S) indicates that N is highly depleted relative to H, C, and S, in the bulk silicate Earth (BSE) reservoir when normalized to CI chondrites (Halliday, 2013; Marty, 2012). This depletion could result from core formation, volatile loss associated with atmospheric evolution or early solar system processes (e.g., Bergin et al., 2015). The exact nature of the source, the mechanisms involved and the timing of VSE delivery to the planet remain debated topics (e.g. Albarède, 2009; Braukmüller et al., 2019; Hirschmann, 2016; Holzheid et al., 2000; Marty, 2012; Wang and Becker, 2013). Regardless of

42 these uncertainties, the partitioning of N in MO-core interactions and the associated backreactions
43 is key to understanding how N gets distributed in both the smaller differentiated impactors that
44 likely delivered volatiles as well as in large terrestrial planets like Earth, which experienced core
45 formation up to extreme PT conditions associated with the later giant impact stages.

46 In this context, there has been significant work towards understanding how nitrogen
47 behaves in metal (core) - silicate (magma ocean) systems that offer insight on the siderophilicity of
48 nitrogen, particularly at lower PT conditions, typically below 20 GPa (Dalou et al., 2019, 2017;
49 Grewal et al., 2022, 2021, 2019a, 2019b; Jackson et al., 2021; Li et al., 2023, 2016; Roskosz et al.,
50 2013; Shi et al., 2022; Speelmanns et al., 2019). Beyond this pressure range, data are sparse and
51 are primarily derived from two studies using laser heated diamond anvil cells (LH-DAC) to
52 investigate metal-silicate reactions (Huang et al., 2024; Jackson et al., 2021). While these LH-
53 DAC data provide insights into the behavior of nitrogen under high PT conditions, they struggle
54 to independently constrain the effects of pressure-temperature-compositional (PTX) parameters.
55 The inherent covariance of PTX parameters in LH-DAC experiments complicates the
56 interpretation of nitrogen partitioning between metal and silicate. To address this, more
57 independent datasets from LH-DAC experiments covering non-overlapping PTX domains are
58 necessary. Such datasets can help confirm the consistency of PTX parameter effects or isolate the
59 impact of each parameter, thereby improving the accuracy of nitrogen behavior predictions under
60 high and extreme core formation conditions.

61 Without the ability to confidently predict the siderophilicity of nitrogen over the full range
62 of pressures, temperatures, and compositions that prevailed during core formation, we cannot
63 know how Earth's accretionary period set the abundance of nitrogen in the mantle which was
64 eventually available to support habitability. Towards this end, we ran high *PT* multi-anvil (MA)
65 and laser heated diamond anvil cell (LH-DAC) experiments to better constrain nitrogen's
66 partitioning during the extreme conditions of core formation. We ran experiments between 15 GPa
67 and 103 GPa with temperatures up to 5600 K and oxygen fugacity ranging between -2.5 to -1 Δ IW
68 to determine the effects of pressure, temperature, oxidation state, and composition on nitrogen's
69 partitioning. We conclude by applying our data to predict VSE fractionations in deep magma
70 oceans.

71 2. Methods

72 We designed a series of laser heated diamond anvil cell (LH-DAC) experiments to test the
73 effect of pressure, temperature, silicate and alloy melt composition, and oxygen fugacity of the
74 system on nitrogen partitioning between metal-silicate ($D_N^{m/s}$) (Table 1). Additionally, we ran a
75 multi-anvil (MA) experiment at 15 GPa to test the efficacy of our nitrogen partitioning model
76 based on previously reported high pressure LH-DAC experiments (>20 GPa), low pressure piston
77 cylinder, MA experiments (<20 GPa) and our new experiments. The different experimental setups
78 and their compositional designs are discussed below.

79 2.1 Starting compositions

80 We utilize a variety of starting compositions to explore the effect of composition (X) on
81 the partitioning of nitrogen. Our nominal silicate composition is adapted from the primitive

82 MORB chemistry from Hirschmann et al. (1998) (62a, Appendix A). We modify their
83 composition to a relatively high Mg# (0.83 compared to 0.77) and no alkali elements. We make
84 these modifications to enable exploration of compositional effects around a relatively
85 undifferentiated mantle composition (e.g. Green and Ringwood, 1963). The mixture (SAMCF in
86 Fig 2.1) was prepared by mixing oxides of SiO₂, Al₂O₃, FeO, and MgO. FeO was prepared from
87 Fe₂O₃ by reducing it in a gas mixing furnace at 1773 K under QFM oxygen fugacity (f_{O_2}) for 45
88 minutes. An alumina crucible was used for doing this reduction. CaO was added after
89 decarbonating CaCO₃ at ~1073K for 2-3 hours. The mixture was homogenized using mortar and
90 pestle, and ball-milled in an alumina crucible for 30 minutes. Ball-milling led to additional
91 alumina getting added to our starting composition. This contamination was up to 5 wt% as
92 measured using EDS in an alumina free starting composition that was ball-milled for 30 minutes.
93 We accounted for this contamination when making our starting mixture, although the
94 contamination does lead to variations in the alumina content of our experimental melts
95 (discussed later).

96 Post ball-milling, 25-30 mg of the mixture was then melted in a gas mixing furnace at
97 1600 K on a rhenium wire loop and at f_{O_2} equivalent of QFM for 30 minutes. The f_{O_2} ensured a
98 dominant divalent Fe in the melt to facilitate later equilibration with Fe alloy (O'Neill, 1987). The
99 melt (glass) bead was then embedded in epoxy and evaluated for homogeneity. We used a Hitachi
100 S-3400 SEM and energy dispersive spectroscopic (EDS) analysis to evaluate and validate the
101 homogeneity of synthesized silicate glass and the absence of quench crystals. Additionally, we
102 created silicate compositions for our f_{O_2} series of experiments (Table 1) by modifying the nominal
103 silicate composition with variable FeO contents (1 and 4 wt%). Finally, we used iron nitride (Fe₂-
104 ₄N) for our metallic-alloy composition, and source of N (7.47 wt% nitrogen), in all our
105 experiments.

106 *2.2 Laser heated diamond anvil cell experiments*

107 After preparing our starting compositions, we assembled the diamond anvil cells (DAC) at
108 Tulane University. Figure 1a shows a schematic cross section of the symmetric DAC assembly
109 with a loaded sample (silicate-alloy). We used diamond culet diameters between 400-200 μ m to
110 compress our samples over the span of our targeted high pressures. The seats holding the diamonds
111 were made of tungsten carbide on both the piston and cylinder sides. The gasket was prepared by
112 pre-indenting a rhenium (Re) foil to ~25-30 μ m. The desired thickness was created by tracking
113 ruby fluorescence during compression (Mao et al., 2008; Shen et al., 2020). We then created the
114 sample chamber by using a micro-laser cutter to drill a cylinder into the pre-indented Re foil such
115 that it aligns centrally with the axes of the diamonds. The fractional diameter of the sample
116 chamber was between 0.33-0.66 of the culet diameters, with the choice depending on the
117 experimental pressure.

118 The starting materials were then prepared to be loaded into the sample chamber.
119 Preparations involved making discs of starting materials (silicate glass, metallic alloy, MgO
120 powder, silicate+metallic alloy mix) which were then stacked into the sample chamber depending
121 on the stack design (Fig 2). To make the silicate discs, we embedded our silicate glass into epoxy
122 and polished it to a thickness of ~10-15 μ m. This thin layer of silicate glass was then laser cut to

123 match the diameter of our sample chamber. For the metallic alloy discs, we compressed Fe₂₋₄N
124 powder using a diamond anvil to ~7-10 μm thickness, and laser cut alloy discs to match the sample
125 chamber diameter. Additionally, MgO discs and discs of the silicate+metallic alloy mix were
126 prepared for our MgO-saturated experiments and are described below. The laser cut discs were
127 then loaded into the sample chambers guided by different designs as explained below.

128 *2.3 Layer designs for experiments*

129 The layer designs in our sample chambers were adapted from our previous LH-DAC
130 studies (Jackson et al., 2021, 2018). We planned two different designs for our experiments, a
131 nominal design (silicate glass-metallic alloy-silicate glass) that was used for the pressure series
132 and a MgO-(silicate+ metallic alloy mix)-MgO design (MgO-saturated experiments) that was run
133 to test the effect of melt composition on $D_N^{m/s}$ (Figure 1b, c). The nominal layer design for our
134 DAC experiments has an iron nitride disc sandwiched between silicate glass discs (Figure 1b). The
135 glass discs provided thermal and chemical insulation of the metal from the diamonds. Besides
136 running our pressure series using this design, we also ran a few experiments with different glass
137 compositions (variable FeO composition) to explore variations in oxygen fugacity of the system
138 (see Table 1 and results). For the MgO-(silicate+alloy)-MgO designs (Figure 1c), we mixed the
139 silicate and the metallic alloy powders in a 2:1 ratio (wt%) and made discs of 10-15 μm thickness.
140 A disc of this mixture is sandwiched between discs of MgO that were prepared by compression to
141 10-15 μm thickness and were laser cut as well. Often the laser cut MgO discs were not coherent,
142 and their shapes needed modification using a tungsten needle to fit the sample diameter.

143 To explore the effect of nitrogen concentration on the partitioning of nitrogen, we modified
144 the alloy by mixing different proportions of Fe₂₋₄N and Fe powders. However, such mixtures
145 suffered from a lack of uniform grain size distribution when mixed using the alumina ball-mill and
146 had larger Fe grains that resulted in inefficient heating and failure during experimentation. This
147 prevented us from systematically evaluating the effect of nitrogen concentration on its partitioning
148 in our experiments.

149 The assembled DACs were heated in a vacuum oven at 393 K for 12-24 hours to remove
150 moisture absorbed by hygroscopic components in the sample chamber. The DACs were then sealed
151 off from moisture by compressing them to ~2-5 GPa.

152 *2.4 Laser heating*

153 The assembled and sealed off DACs were laser heated at GSECARS (13-ID-D beamline,
154 Advanced Photon Source, Argonne National Lab) to react N-bearing metal and silicate under PT
155 conditions highlighted in Table 1. Specific target pressures were reached and monitored using
156 diamond edge Raman measurements (Akahama and Kawamura, 2006; Dobrosavljevic et al.,
157 2023). We recorded the average pressure of the sample chamber and the associated standard
158 deviation after each heating cycle using diamond edge. During each heating cycle, we used the
159 XRD measurements of mineral phases (e.g., Fe, MgO) with known equations of state to estimate
160 pressure (Fig S-2) (Ono et al., 2010; Sha and Cohen, 2010; Wu et al., 2008). Integration of XRD
161 images and visualization was done using the software DIOPTAS (Prescher and Prakapenka, 2015).

162 We used a focused $\sim 15\text{-}20\ \mu\text{m}$ IR laser beam to heat our samples, coupled from both
163 upstream and downstream sides of the DAC. We first annealed each experiment at $\sim 1500\text{-}1800\ \text{K}$
164 to lower any existing pressure gradients within the sample chamber and to identify regions that
165 coupled well with the laser. Selected regions were then heated in a new heating cycle. To heat, we
166 manually controlled the power ramp on the upstream (US) and the downstream (DS) side steadily
167 up to $\sim 2000\ \text{K}$ while maintaining minimal temperature difference between the two sides.
168 Temperatures were measured from wavelength of the incandescent radiation from heating the
169 sample which was generally between $660\text{-}780\ \text{nm}$. Temperature measurements were processed
170 using T-rax (software by C. Prescher; github.com/CPrescher/T-Rax) that allowed for selection of
171 more accurate wavelength windows that best described a grey body fit of the incandescent intensity
172 (Table S-1). Around $2000\ \text{K}$, we rapidly increased power input until melting was achieved. Melting
173 was confirmed by in-situ XRD measurements, which collect diffraction peaks of phases while
174 heating the sample. Melting was also visually confirmed by a sudden increase in the incandescence
175 of the samples. Some experiments displayed flickering incandescence at higher powers. Many
176 hotspots that displayed flickering later had uncontrolled temperature drops and associated heating
177 failures. Such experiments were not included in our dataset. After confirmation of melting, we
178 acquired repeat measurements of the temperature to confirm temperature stability during the
179 molten state of the heating-spot along with their corresponding XRD measurements. Finally, the
180 sample was quenched by cutting off laser power. The high conductivity of diamond was
181 instrumental for rapid heat loss and quenching. Each heating cycle typically lasted several minutes,
182 with the heating-spots maintained at peak or near-peak temperatures for at least 10 seconds (Figure
183 2).

184 Experimental temperature estimates provided in Table 1 are the average temperatures of
185 the final melting temperature measurements (before quenching) collected on the upstream and the
186 downstream sides. Note that each temperature measurement collected on either the upstream or
187 the downstream are averages from a series of rapid measurements of the sample incandescence at
188 the time of collection. The uncertainties of the temperature readings in Table 1 are the combined
189 standard deviations of the final series of measurements taken on the upstream and the downstream.
190 The recorded melting temperatures were used to account for thermal pressure ($\Delta P_{\text{th}} = 2.7\ \text{MPa/K}$,
191 from Siebert et al., 2012) which is added to the recorded diamond edge pressure post heating to
192 get the final pressures reported in Table 1.

193 *2.5 DAC sample preparation for microprobe analysis*

194 The DAC samples were then steadily decompressed at Tulane and preparations
195 commenced for their chemical analysis. We first laser cut the Re around sample chambers to
196 separate them from the remaining gasket, creating a disc nearly the diameter of the diamond culet.
197 Marks for orientation were made on the Re portion of the discs and the discs were mounted on a
198 TEM grid using a tungsten needle.

199 The heated spots (ref. as hot-spot) on these mounted samples were then cut open to expose
200 a cross section that revealed the synthesized phases. This second step was done at LSU by using a
201 focused ion beam (FIB) with a Ga source (Quanta 3D Dual Beam FEG FIB-SEM) and a plasma
202 focused ion beam (PFIB) with a Xe source (Helios G5 CXe Plasma FIB). Both the instruments

203 accelerate focused ions to mill the sample and explore the exposed cross sections. The PFIB was
204 effective in making larger, coarser cuts at a 60 nA, 30 KeV ion beam current. This allowed for
205 faster removal of the un-melted sample region. The Ga-FIB was then used to make smaller but
206 finer cuts at 1-15 nA and 30 KeV ion beam current. The finer cuts allowed for a more careful
207 survey of the phases being exposed when approaching a hot-spot. Exposure of a hot-spot (Figure
208 3) was confirmed with secondary electron images.

209 *2.6 Multi-anvil experiment*

210 In addition to the DAC experiments, we ran a multi-anvil (MA) experiment at 15 GPa and
211 2773 K to corroborate our results obtained from LH-DAC experiments. We followed the sample
212 assembly technique outlined in Righter et al. (2020) and ran the experiment in the 880 ton multi-
213 anvil press at JSC using a 10/5 octahedra assembly. For our starting composition, we used the same
214 2:1 ratio of silicate+metallic alloy mix that was used for our MgO-saturated LH-DAC experiments.
215 Additionally, we added a 1 wt% Si to the metallic alloy (Fe₂₋₄N) to facilitate metal saturation. We
216 loaded this starting composition into a single crystal MgO capsule. The sample was then heated
217 following previously established power-temperature curves for the specific press and the sample
218 assembly that we utilized (Fig S-1). Temperature was monitored using a type C W/Rh
219 thermocouple up to a reading of 2373 K at which the thermocouple signal was lost. Heating of our
220 sample beyond 2373 K to 2773 K was estimated using the resistivity of the heater, output power,
221 and previous temperature calibration experiments on the same instrument. The experiment was
222 held at 2773 K for ~5 minutes and quenched by shutting off power to the sample heating assembly.
223 The quenched sample was later embedded in epoxy and polished using diamond pastes of
224 increasing grit (up to 5000 grit or ~2 um) for microprobe analysis.

225 *2.7 Electron Microprobe Analysis*

226 The exposed phases were analyzed for their silicate and alloy compositions at JSC using a
227 JEOL 8530F Electron Probe Micro Analyzer. All samples were coated with Ir or Pt to facilitate the
228 analysis of C. Prior to coating, each DAC sample was finely polished using a Ga-FIB (Quanta 3D)
229 at low current. This polishing step was taken to remove any contaminants that had potentially
230 accumulated on the surface since their initial milling and to further polish the sample surface.
231 Polishing was completed with a 1 nA, 30 KeV ion beam. Once samples were polished and coated,
232 they were loaded into the vacuum chamber of the electron microprobe to limit accumulation of C,
233 O, or H on the sample surfaces prior to their analysis.

234 Primary standards used for calibration were anorthite (for Al, Ca), San Carlos olivine (for
235 Si, Mg), fayalite (for Fe, Si), stainless steel (for Fe, Ni), Si₃N₄ (for N), Fe₃C (for C), and magnetite
236 (for O). Peak intensities for elements of interest were quantified and were corrected for background
237 X-ray intensity. Background was obtained through linear fitting of background intensity around
238 the peaks of elements. Backgrounds and peak positions for light elements (N, C, O) used to
239 quantify their concentrations are shown in Fig S-3. Count times for nitrogen was 90s at peak
240 position and 60s for background, while that for other elements were 30s and 15s, respectively. We
241 also analyzed the secondary standards, including volcanic glass (VG2), fayalite, San Carlos
242 olivine, hyalophane, diopside, and magnetite. All secondary standards except hyalophane are

243 Smithsonian microbeam standards. Nitrogen was measured on Hyalophane at 0.11+- 0.02 wt%
244 compared to a value of 0.12 wt% reported by Beran et al. (1992). We also analyzed stainless steel
245 to measure the analytical precision and accuracy for alloy forming elements (C, N, Si). The blank
246 concentration of nitrogen was <0.01 wt% measured on nominally nitrogen free secondary
247 standards magnetite, fayalite, diopside and San Carlos olivine. We then analyzed our samples for
248 SiO₂, Al₂O₃, FeO, MgO, CaO, N, and C in the silicate phases and Si, Al, Fe, Mg, Ca, N, C, and O
249 in the metallic phases. Most analysis used a 10 KeV accelerating voltage and a beam current of 10
250 nA with a beam diameter of 1 μm for the analysis of both silicate and metal phases. We also used
251 variable beam current (3nA and 5 nA) to confirm that nitrogen was not mobilized with variable
252 beam densities.

253 3. Results

254 3.1 Experimental phases stabilized

255 We ran experiments as a pressure series and a compositional series (Table 1) to understand
256 the effects of PTX on the partitioning of nitrogen between metal-silicate. Although we start with
257 fixed bulk initial silicate and metal compositions within the respective designs (Figure 2b and c),
258 we get a wide variation in the silicate and the metal compositions across our samples post
259 experimentation (Table 1, Figure 3.3). This is likely caused from the small variations introduced
260 to the silicate compositions from alumina contamination during ball milling, the variable PT
261 conditions of our experiment, and the local compositional domain sampled by the laser beam (~15-
262 20 μm).

263 The experiments with both designs (Figure 2 b and c) had a silicate phase (magma ocean
264 equivalent) and a metallic phase (core) at the center of each hot-spot (Figure 3), but the different
265 designed yielded different textures, mineral phase assemblages surrounding the quenched silicate,
266 and major element chemistries. The MgO-saturated experiments often had a layer of ferropericase
267 and/or bridgmanite encapsulating the silicate and metal phases (Figure 3a). These experiments had
268 depolymerized silicate melts with NBO/T values between 2.7 – 3.7 and were often associated with
269 relatively coarse quench textures in both the metallic and the silicate phases (Figure 3 a,b).
270 Analysis of nitrogen concentrations in these silicate melts varied between 0.6-0.8 wt%, while the
271 associated metallic domains had higher nitrogen concentrations between 4.7-10 wt%. In
272 comparison, the nominal DAC designs had their metal and silicate phases mantled by a CaSiO₃-
273 rich layer, likely davemaoite at the PT conditions of our experiments (Figure 3b, Table 1). These
274 experiments had more polymerized silicate melts with NBO/T ranging between 0.5- 1.1. In
275 addition, a stark difference between the two designs was also reflected in the O and the Si contents
276 of the metallic domain, where the MgO saturated experiments had more O (up to 7 wt%), but the
277 nominal designs had more Si content (up to 9.5 wt%). This gave us a wide range of light element
278 concentrations (O, Si) in our metallic domains over a relatively narrow PT space that enables us
279 to more directly explore the effects of these elements on nitrogen siderophility. Carbon was present
280 in our experiments, likely introduced as a contaminant, with up to 5.79 wt% in the metal, after
281 removing blank concentrations of ~0.02 wt% measured on stainless steel.

282 The multi-anvil experiment (Figure 4) was MgO-saturated and displayed prominent
283 quench textures with metallic blobs (<1 μm to 100s of μm in diameter) amidst the silicate mass.
284 The relative coarse quench texture likely reflects the slower quench and relatively depolymerized
285 composition of this experiment with an NBO/T value of 2.67. The silicate had elongated crystals
286 of MgO and (Mg,Ca) SiO_3 as seen in previously run MgO-saturated MA experiments (e.g., Righter
287 et al., 2020). Although we analyzed silicate domains that had relatively fine crystals, the major
288 element concentrations (in wt%) of FeO, CaO and Al_2O_3 had higher standard deviations (>0.5
289 wt%) than that found in secondary standards (<0.4 wt%). The MgO and the SiO_2 contents (wt%)
290 across the silicate phase had the most variation with standard deviations 3.5 wt% and 1.8 wt%,
291 respectively which was likely due to sampling of different proportions of quench crystals. Nitrogen
292 and carbon had a similar standard deviation (0.17 wt% and 0.26 wt%, respectively) across the
293 silicate domain as found in the secondary standards (up to 0.14 wt% and 0.20 wt%, respectively).
294 The average nitrogen concentration across the silicate domain was 0.31 wt%. For the metallic
295 analysis, we measured blobs that were between 5-100 μm in diameter (Figure 4). The metal
296 analysis showed more consistent concentrations of elements across the blobs with a maximum
297 standard deviation of 0.42 wt% for the Fe concentration. The concentrations of Si, Al, Mg, and Ca
298 were <0.1 wt%, while the average nitrogen concentration in the metal 10.23 wt% with a standard
299 deviation of 0.41 wt%. The measured oxygen concentration was below the blank concentration of
300 0.43 wt% measured on stainless steel.

301 *3.2 PTX space explored by our new high-pressure data*

302 We conducted successful experiments that investigated nitrogen partitioning between metal
303 and silicate under previously unexplored PTX conditions (Figure. 5). It is important to note that
304 PTX variables co-vary in our experiments, and any observed trends in Figure 5 are likely
305 influenced by these interdependencies. Our new high-pressure data spans a range of 15-103 GPa,
306 similar to a recent study by Huang et al. (2024). However, our experiments achieved metal-silicate
307 equilibrium over a broader temperature range and higher temperature (2573-6466 K, Figure 5a).

308 Oxygen fugacity in our experiments showed variations of 1.5 log units with respect to the
309 IW oxygen buffer (calculation described below, Figure. 5b). This range is likely influenced by the
310 experimental temperature and the varying abundance of oxidized and reduced compounds in the
311 laser-heated region, some of which may be contaminants (e.g., H_2O , organic carbon, FeO, Fe). Our
312 experiments produced a diverse range of silicate melts (Figure 5c), enabling us to investigate the
313 effect of silicate melt chemistry on nitrogen partitioning.

314 The metallic domains synthesized under these high PT conditions allowed for greater
315 incorporation of light elements (Si, O) into the alloy than previously explored (Figures 6a, b; 5d,
316 e). Additionally, our metallic chemistry also captured higher than previously explored nitrogen
317 concentrations (Fig 5f) likely due to nitrogen added as Fe_{2-4}N in our starting composition.

318 *3.3 Determination of oxygen fugacity*

319 Oxygen fugacity of our LH_DAC experiments span between $\Delta\text{IW}-1.03\pm 0.02$ and $\Delta\text{IW}-$
320 2.51 ± 0.06 and was estimated using the equation below, where ΔIW represents $f\text{O}_2$ calculated as
321 log unit deviation from IW oxygen buffer.

322 $\Delta IW = 2 \log \left(\frac{x_{FeO}^{silicate} \gamma_{FeO}^{silicate}}{x_{Fe}^{metal} \gamma_{Fe}^{metal}} \right)$

323 The mole fractions of FeO and Fe are determined from analysis. We assume a γ -FeO of
 324 1.25, similar to what was reported by O'Neill and Eggins, (2002) for a MORB system. This
 325 assumption is used for our own data and the literature data when computing ΔIW and
 326 parameterizing for $D_N^{m/s}$ values below. The γ -Fe of our metallic alloy was evaluated using the Ma,
 327 (2001) formalism. This approach enables the application of interaction coefficients for alloying
 328 elements (Si, C, S, O) in predicting the non-ideality of Fe in Fe alloy. We use the interaction
 329 parameters (ϵ) for Si-Si, C-C, S-S, O-O, Si-C, Si-O, Si-S, C-O, C-S and O-S interactions from
 330 Badro et al. (2018). The equation below shows how γ -Fe is calculated for a N component metallic
 331 solution with Fe as the solvent and N-1 solutes (Si, C, S, O).

332
$$\ln \gamma_{Fe} = \sum_{i=1}^{N-1} \epsilon_i^i (X_i + \ln(1 - X_i)) - \sum_{i=1}^{N-2} \sum_{j=i+1}^{N-1} \epsilon_i^j X_i X_j \left(1 + \frac{\ln(1 - X_i)}{X_i} + \frac{\ln(1 - X_j)}{X_j} \right)$$

333
$$+ \sum_{i=1}^{N-1} \sum_{\substack{j=1 \\ (j \neq i)}}^{N-1} \epsilon_i^j X_i X_j \left(1 + \frac{\ln(1 - X_j)}{X_j} - \frac{1}{(1 - X_i)} \right)$$

334
$$+ \frac{1}{2} \sum_{i=1}^{N-2} \sum_{j=i+1}^{N-1} \epsilon_i^j X_i^2 X_j^2 \left(\frac{1}{1 - X_i} + \frac{1}{1 - X_j} - 1 \right)$$

335
$$- \sum_{i=1}^{N-1} \sum_{\substack{j=1 \\ (j \neq i)}}^{N-1} \epsilon_i^j X_i^2 X_j^2 \left(\frac{1}{1 - X_i} + \frac{1}{1 - X_j} + \frac{X_i}{2(1 - X_i)^2} - 1 \right)$$

336

337 3.4 Equilibrium check

338 We evaluate equilibrium in our experiments by **A**) comparing the distributions of Si, O,
 339 and Mg in our experiments with literature predictions, **B**) evaluating the spatial variation of major
 340 and minor element compositions across metal and silicate domains, and **C**) evaluating the
 341 characteristic diffusion length scales of elements in our experiments.

342 **A)** We explore the distribution of Si, O, and Mg in our metal-silicate experiments which
 343 have been well characterized up to high PT conditions (Badro et al., 2018; Fischer et al., 2015).
 344 Strong temperature dependency has been observed in the exchange coefficients of Si and the
 345 equilibrium constant associated with the dissociation of MgO (Badro et al., 2018; Fischer et al.,
 346 2015), while O has been suggested to exhibit both pressure and temperature dependencies on its
 347 metal-silicate partitioning (Fischer et al., 2015). Comparing the distribution of these elements in
 348 our experiments with predictions from the literature allowed for the evaluation of the accuracy of
 349 our chemical analysis and temperature determinations.

350 KD-Si (exchange coefficient for Si and Fe between metal and silicate) was determined
351 given the following reaction: SiO_2 (silicate) + 2Fe (metal) = 2FeO (silicate) + Si (metal). Without
352 any compositional recalculations (Figure 6a inset), our data have a similar temperature dependency
353 compared to the Fischer et al. (2015) model prediction but generally scatter below the model slope.
354 We recalculate raw (no recalculation) KD-Si values considering Si-O and Si-C interactions using
355 ϵ parameters from Fischer et al. (2015) and Steelmaking Sourcebook (1988), respectively. The
356 recalculated KD-Si values have small deviations from the raw values (Figure 6a main). Note that
357 our comparison in Figure 6a does not account for the effect of Si-N interactions, and this effect is
358 discussed below. The general scatter below the model prediction is consistent with Si repelling N
359 in Fe alloy.

360 Values of KD-O were computed based on the dissociation reaction: FeO (silicate) = Fe
361 (metal) + O (metal). Compositionally recalculated values are plotted in Figure 6b (main), while
362 raw KD-O values are plotted in the inset, (Figure 6b inset). Our KD-O values are correlated with
363 temperature, with higher temperature being associated with higher KD-O values, but our data do
364 tend to plot below the isobars associated with our experimental pressures for both recalculated and
365 raw data. Compositional recalculation of KD-O values account for O-Si, O-C, and O-O
366 interactions using the ϵ parameters from Fischer et al. (2015) and Badro et al. (2015). As with Si,
367 our comparison of KD-O values does not account for the effect of O-N interactions. The general
368 scatter below the model prediction is consistent with O repelling N in Fe alloy, as discussed below.

369 We also compared the KD-Mg in our experiments with model predictions from Badro et
370 al. (2018). We determined KD-Mg based on the MgO dissociation reaction, where MgO (silicate)
371 = Mg (metal) + O (metal). Values of KD-Mg were recalculated for Mg-O, Mg-Si and Mg-C
372 interactions using ϵ parameters from the same work. There is good agreement of our recalculated
373 KD-Mg values with the model slope (Figure 6c). One exception is N49-2 for which both the
374 calculated exchange coefficients of Si and the equilibrium constant for the dissociation of MgO
375 suggest colder temperatures than what we determined, scattering beyond the remainder of the data.
376 This sample was therefore rejected from the dataset used for parameterizing $D_N^{m/s}$ values. Taken
377 together, our evaluations of Si, O, and Mg distributions in our experiments suggest that major
378 element exchange between the metallic and silicate domains was efficient at our estimated
379 temperatures and closely approach equilibrium conditions.

380 **B)** Another line of evidence for a close approach to equilibrium comes from the evaluation
381 of compositional variation across the metal and the silicate domains in our experiments (Figure 7)
382 using WDS and EDS (Figure 3). Under equilibrium conditions, there should be uniform
383 compositions of the different phases in the assembly at a fixed PTX. Using WDS, we see variability
384 between individual analysis of any given phase beyond the analytical precision of the microprobe
385 (Figure 7). This is likely due to sampling of quenched crystals by the electron beam within
386 respective silicate and metallic domains. Quench crystals tend to form in both our experimental
387 designs, with more depolymerized designs having coarser quench crystals. However, the average
388 concentration of an element measured from multiple analysis across any given phase likely
389 approaches the true chemistry of the phase. This is reflected in the equilibrium distribution of Si,
390 Mg, and O between the metallic and the silicate domains as discussed above (Figure 6). However,

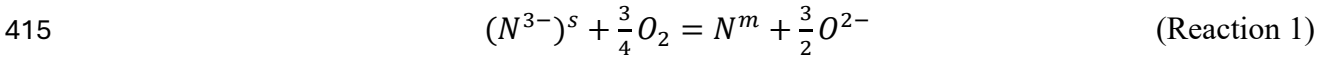
391 there is not any systematic variation of composition across the overall domains that would indicate
 392 disequilibrium conditions.

393 C) We calculate the characteristic diffusion length scales for major elements in our metallic
 394 and silicate domains as a final evaluation for the approach to equilibrium in our experiments. Each
 395 experiment starts with unreacted materials that must exchange chemistry at high PT conditions to
 396 approach equilibrium over the heating duration. We calculate the diffusion lengthscale using $L =$
 397 $2\sqrt{Dt}$, where D is the diffusion coefficient of an element and t is time. The large majority of our
 398 experiments were conducted above 4000 K and below 100 GPa, and within this PT window the
 399 diffusion coefficients of Mg, Si, and O are all found to be near 10^{-9} m²/s or faster (Karki et al.,
 400 2010). Heating durations for our experiments varied but were always greater than 10s (Figure 2).
 401 The implied minimum diffusion length scale is 63 μm in silicate. Similarly, diffusion coefficients
 402 for liquid Fe alloy are estimated to be 10^{-7} m²/s or larger for the PT conditions of our experiments
 403 (Huang and Badro, 2018). The implied minimum diffusion lengthscale for major elements in our
 404 alloy is 200 μm. In comparison the dimensions of our silicate and melt phases (~5-20 μm) are
 405 always smaller than our calculated diffusion lengthscales, and this suggests that heating durations
 406 of our experiments were sufficiently long enough for metal and silicate domains to exchange
 407 elements and approach equilibrium.

408 4. Discussion

409 4.1 Theoretical basis for parameterization of $D_N^{m/s}$

410 As established above, our dataset has expanded the PTX coverage of existing data for $D_N^{m/s}$
 411 values, and this permits the parameterization of these data to describe how $D_N^{m/s}$ values vary in
 412 response to changes in intensive thermodynamic properties. Towards this end, we first assume that
 413 nitrogen in the silicate exists as N^{3-} as suggested by Libourel et al. (2003) for systems more
 414 reducing than IW and partitions as neutral N into the metal following the reaction below:



416

417 The equilibrium constant for this reaction can be written as:

$$418 \quad K_N = \frac{(\gamma_N^m X_N^m)(aO^{2-})^{\frac{3}{2}}}{(\gamma_{N^{3-}}^s X_{N^{3-}}^s)(fO_2)^{\frac{3}{4}}} = \frac{(\gamma_N^m)(aO^{2-})^{\frac{3}{2}}}{(\gamma_{N^{3-}}^s)(fO_2)^{\frac{3}{4}}} D_N^{\frac{m}{s}}, \text{ or}$$

$$419 \quad \ln K_N = \ln \gamma_N^m - \ln \gamma_{N^{3-}}^s + \ln D_N^{\frac{m}{s}} - \frac{3}{4} \ln (fO_2) + \frac{3}{2} \ln (aO^{2-}) \quad (\text{eq 1})$$

420 where X_N^m and $X_{N^{3-}}^s$ are mole fractions of nitrogen in the metal and silicate respectively and γ_N^m and
 421 $\gamma_{N^{3-}}^s$ are the corresponding activity coefficients. $D_N^{\frac{m}{s}}$ is the partition coefficient of nitrogen between
 422 metal and silicate and is expressed as $D_N^{\frac{m}{s}} = \frac{X_N^m}{X_{N^{3-}}^s}$. fO_2 is the oxygen fugacity of the system. We
 423 assume the activity of oxygen anion (aO^{2-}) in the silicate melt to be a constant.

424 By definition, equilibrium constant can be written as:

$$425 \quad -K_N = \exp\left(\frac{\Delta H^o}{RT} - \frac{\Delta S^o}{R} + \frac{P\Delta V^o}{RT}\right) \quad (\text{eq 2})$$

426 Here, K_N is the equilibrium constant of reaction 1, ΔH^o , ΔS^o , and ΔV^o are the standard enthalpy
427 change, entropy change and volume change of the reaction, R is the gas constant in J/mole/K, and
428 T is temperature in K.

429 From Eq 1 and Eq 2 and with an assumption that ΔH^o , ΔS^o , and ΔV^o are constant across changes
430 in P and T, $D_N^{\frac{m}{s}}$ can be re-cast as:

$$431 \quad \ln D_N^{\frac{m}{s}} = a\frac{1}{T} + b\frac{P}{T} + c + \frac{3}{4}\ln(fO_2) - \ln\gamma_N^m + \ln\gamma_{N^{3-}}^s \quad (\text{eq 3})$$

432 γ_N^m can be computed using the Ma (2001) approach for a ‘N’ component system with Fe as the
433 solvent and ‘n-1’ solutes:

$$434 \quad \ln\gamma_N^m = \ln\gamma_{Fe}^m + \ln\gamma_N^o - \frac{T_{ref}}{T}\varepsilon_N^N \ln(1 - X_N) - \sum_{\substack{j=1 \\ (j \neq N)}}^{n-1} \varepsilon_N^j X_j^{m'} \quad (\text{eq 4})$$

435 Where γ_N^o represents the activity coefficient of nitrogen in the metal at infinite dilution, ε_N^N is the
436 nitrogen self-interaction parameter and ε_N^j is the interaction parameter for the elements $j = C, S,$
437 Ni, O or Si influencing nitrogen activity in the metal. $T_{ref} = 1873$ K, the reference temperature at
438 which most steelmaking ε values are reported. $X_j^{m'}$ takes the form:

$$439 \quad X_j^{m'} = \frac{T_{ref}}{T} \left[\sum_{\substack{j=1 \\ (j \neq i)}}^{n-1} \varepsilon_i^j X_j \left(1 + \frac{\ln(1-X_j)}{X_j} - \frac{1}{(1-X_i)} \right) - \sum_{\substack{j=1 \\ (j \neq i)}}^{n-1} \varepsilon_i^j X_j^2 X_i \left(\frac{1}{1-X_i} + \frac{1}{1-X_j} + \frac{X_i}{2(1-X_i)^2} - 1 \right) \right] \quad (\text{eq 5})$$

441 where $X_{i,j}$ are mole fractions of the different elements in the alloy.

442 We assume $\gamma_{N^{3-}}^s$ follows a symmetric regular solution model (e.g. Ghiorso and Carmichael, 1980):

$$443 \quad \ln\gamma_{N^{3-}}^s = \frac{\omega_N^i(X_i)^2}{RT} \quad (\text{eq 6})$$

444 for a binary $N^{3-} - i$ solution where i is a silicate melt component and X_i represents the mole fraction
445 of this component other than N^{3-} . ω_N^i is the regular solution parameter for this interaction, R is the
446 gas constant in J/mole/K, and T is temperature in K.

447 4.2 Model formulation:

448 Eq 3 gives us the functional forms of PTX parameters that can explain the partitioning of
449 nitrogen between metal and silicate. We then compiled a global dataset (Dalou et al., 2019, 2017;
450 Grewal et al., 2022, 2021, 2019a, 2019c; Huang et al., 2024; Jackson et al., 2021; Li et al., 2023,
451 2016; Roskosz et al., 2013; Shi et al., 2022; Speelmanns et al., 2019) to parameterize $D_N^{m/s}$ over a
452 wider span of PTX conditions than what our study alone enables. For the Roskosz et al. (2013)

453 dataset we assume zero carbon concentrations for the LH-DAC data and assume the deviation of
 454 the totals from 100% as carbon concentrations for the MA experiments. Additionally, we do not
 455 include 7 data points from Grewal et al. (2019a) (discussed in Fig S-4) and one experiment
 456 *PC_N_EXP3* from Jackson et al. (2021) with high Si (~13 wt%) in the metal at 0.95 GPa and 1973
 457 K.

458 Since the alloy effects for N-C, N-S and N-Ni interactions have been systematically studied
 459 in earlier works (e.g., Grewal et al., 2019a, 2019b; Jackson et al., 2021; Roskosz et al., 2013; Shi
 460 et al., 2022), we recalculate the measured $D_N^{m/s}$ values of our global data for these interactions. It
 461 is also necessary to recalculate for these effects considering the absence of these elements in some
 462 experimental studies that we include in our global database and their overall subtle effect on the
 463 global dataset. To recalculate, we subtract the term $\varepsilon_N^j X_j^{m'}$ from the measured $D_N^{m/s}$ (log) using Eq
 464 5 for C, S, and Ni and the interaction parameters from Jackson et al. (2021).

465 The C-, S-, Ni- recalculated D_N values were then fit against the other relevant parameters
 466 based on Eq 3 using a least squares approach. We evaluate the parameters based on their
 467 significance (p-value). The threshold for p-values was set at 0.05, and we did not consider
 468 parameters with >0.05 p-values. We started a model with $1/T$, P/T and fO_2 as our initial set of
 469 parameters based on the thermodynamic rationale presented in Eq 3. Oxygen fugacity, expressed
 470 as ΔIW , had the lowest p-value (<0.0001) and gave an R^2 of 0.62 alone. $1/T$ followed as the
 471 subsequent significant term with a p-value <0.0001 and increased the R^2 to 0.73. Bringing in the
 472 P/T term, however, had a high p-value (>0.05) and was not considered initially for the model.

473 We then explored the significance of different compositional parameters and their effect on
 474 the model fit. For the alloy chemistry effects, we explored the parameters $\ln(1 -$
 475 $X_N) \frac{T_{ref}}{T}$ (annotated as $X_N^{m'}$), $X_O^{m'}$, $X_{Si}^{m'}$, $X_{Mg}^{m'}$, $X_{Ca}^{m'}$, and $X_{Al}^{m'}$ to identify the alloy solute
 476 components that affect $D_N^{\frac{m}{s}}$. The X_j' values ($j = N, O, Si, Mg, Ca, Al$) were calculated using Eq 5.
 477 The terms $X_{Si}^{m'}$ and $X_N^{m'}$ had the highest significance with p-values <0.0001 followed $X_O^{m'}$ with a
 478 p-value of 0.01. $X_{Mg}^{m'}$, $X_{Ca}^{m'}$ and $X_{Al}^{m'}$ had p-values >0.05 and were not included in the model. The
 479 overall model had an R^2 of 0.78 at this step.

480 We evaluated the significance of our oxide parameters ($i=SiO_2, Al_2O_3, MgO$ and CaO) in
 481 their functional form $\frac{\omega_N^i(X_i)^2}{RT}$. We did not fit for FeO given its direct correlation with the ΔIW term,
 482 already included in the model. Amongst our oxide parameters, we found that SiO_2 and MgO have
 483 higher significance (p-values <0.0001) than CaO and Al_2O_3 . The SiO_2 and the MgO contents are
 484 anticorrelated in the experiments and can therefore be used interchangeably to capture the effect
 485 of silicate composition on N. However, choosing either SiO_2 or MgO as the first significant silicate
 486 parameter had implications on the next choice of silicate parameters and on the slope of the already
 487 identified significant parameters. Choosing MgO as the first silicate parameter, CaO and Al_2O_3
 488 followed suit as the next silicate parameters. Each of these terms (MgO, CaO, Al_2O_3) had positive
 489 coefficients, which suggested that their enrichment in the melt makes nitrogen more siderophile.

490 With this choice of silicate parameters, SiO₂ became less significant with a p-value of 0.0206. The
 491 model R² value was 0.87 with this choice.

492 Choosing SiO₂ as the first silicate parameter, on the other hand, yielded a negative
 493 coefficient and suggested that nitrogen becomes less siderophile with SiO₂ enrichment in the
 494 silicate melt. The R² of the model when choosing SiO₂ as the significant silicate parameter was
 495 0.84. Choosing SiO₂ as the silicate parameter decreased the slope of ΔIW from 0.54 to 0.39. This
 496 deviation further away from the ¾ slope is expected for a N³⁻ dominated speciation in the silicate
 497 melt. Given the choice of MgO or SiO₂ to describe melt compositional effects, we selected SiO₂.
 498 Our decision here is driven by evidence for Si-N³⁻ interactions in silicate melts (Huang et al., 2022)
 499 that should act to stabilize nitrogen in the silicate and decrease its siderophility (consistent with
 500 the negative coefficient we retrieve from our fitting).

501 Finally, the P/T term became significant with a p-value of 0.0059 after considering the
 502 compositional terms discussed above, while the overall model R² improved by 0.004. The
 503 significance of this term was independent of our choice for the silicate melt parameter.

504 With the 7 PTX parameters identified from the procedure described above our final model
 505 takes the form in Eq 7 with an R² of 0.84.

$$\begin{aligned}
 506 \quad \log D_N^{\frac{m}{s}} = & \frac{5559.4(\pm 450.6)}{T(K)} + \frac{33.3(\pm 12.0)P(GPa)}{T(K)} + 0.39(\pm 0.02)\Delta IW - 5.46(\pm 1.29)X_N^{m'} + \\
 507 \quad & 8.72(\pm 2.66)X_O^{m'} + 9.05(\pm 1.04)X_{Si}^{m'} - 54023(\pm 5055) \left(\frac{X_{SiO_2}^s}{R.T(K)} \right)^2 - 0.11(\pm 0.22) \quad (\text{eq 7})
 \end{aligned}$$

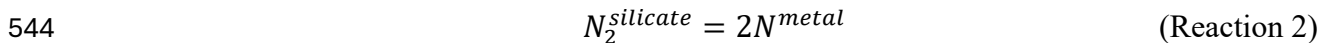
508
 509 Note that Eq 7 is derived for systems without C, Ni, and S. To include these compositional effects
 510 in predictions we suggest adding interaction terms analogous to those given for oxygen or silicon,
 511 although this complicates propagation of uncertainties.

512 *4.3 Model parameters and their implications:*

513 Our model from Eq 7 allows us to understand the behavior of nitrogen during core
 514 formation with the most diverse PTX coverage to date (Figure 3). Based on our model fits, we
 515 infer that pressure has a positive effect on the siderophility of nitrogen, while temperature has a
 516 negative influence on its siderophility (Figure 8a). Our temperature sensitivity is similar to
 517 previous determinations (Grewal et al., 2019a; Huang et al., 2024; Jackson et al., 2021; Shi et al.,
 518 2022; Speelmanns et al., 2019). Although there is uniform agreement that higher temperatures
 519 make N less siderophile, there is more disagreement regarding the role of pressure in modulating
 520 nitrogen partitioning. The models presented by Dalou et al. (2017) and Speelmanns et al. (2019)
 521 suggest negligible pressure effect between 1.2-3 GPa and 0.85-5.5 GPa, respectively, whereas
 522 models by Grewal et al. (2019a, 2019b) (1-6 GPa) and Shi et al. (2022) (1-8 GPa) report a positive
 523 effect of pressure on nitrogen's siderophility. Higher pressure behavior of nitrogen beyond 8 GPa
 524 was explored by Huang et al. (2024), Jackson et al. (2021) and Roskosz et al. (2013) but these
 525 studies had different conclusions on the effect of pressure. While Roskosz et al. (2013) did not

526 observe any conclusive effect of pressure on $D_N^{m/s}$ in their experiments conducted up to ~15 GPa,
527 Jackson et al. (2021) ran experiments between 0.95 -25.6 GPa and their model suggested that
528 pressure increases the siderophilicity of nitrogen. Although, Huang et al. (2024) did not require any
529 pressure effect in their model that included higher PT data up to 104 GPa. Our conclusion regarding
530 the positive effect of pressure on nitrogen partitioning is enabled by the expanded PTX provided
531 by our dataset.

532 We find that oxygen fugacity of the system has a positive effect on nitrogen siderophilicity,
533 meaning more oxidized conditions favor nitrogen siderophilicity (Figure 8b). This relationship
534 qualitatively consistent with Reaction 1 and is consistent with other nitrogen metal-silicate
535 partitioning studies (Dalou et al., 2019; Grewal et al., 2019a; Huang et al., 2024; Jackson et al.,
536 2021; Li et al., 2016; Shi et al., 2022; Speelmanns et al., 2019). The coefficient we find for ΔIW ,
537 however, is 0.39 (± 0.02), much lower than the 0.75 slope predicted by Eq 3 for Reaction 1. A
538 large deviation from the 0.75 slope may suggest the involvement of a N_2 species as a solute
539 component in the silicate phase or the stabilization of N^{3-} by Fe^{+2} dissolved in the melt. There is
540 evidence from molecular dynamical work that N^{3-} does complex with Fe^{+2} and Si^{+4} under PT
541 conditions relevant to this study (Huang et al., 2022). Oxidizing and N-rich conditions promote
542 N_2 stability over N^{3-} and could require a different reaction to constrain nitrogen's partitioning, as
543 below.



545

546 If N_2 dominates the budget of N in melt then N partitioning would become insensitive to
547 oxygen fugacity (Dasgupta et al., 2022; Libourel et al., 2003; Mysen et al., 2014), lowering the
548 coefficient ΔIW . Thus, there should be a PTX boundary where the Eq 7 is no longer valid.
549 Experiments conducted under low PT conditions (up to 10 GPa and 1773 K) identify the redox
550 boundary between N^{3-} and N_2 dominated melt solubility near IW (Libourel et al., 2003), but it
551 has not been defined for the PTX conditions associated with laser heated DAC studies (this
552 study; Huang et al., 2024). Further systematic investigation of high PTX experiments are needed
553 to find such a redox boundary and to evaluate the accuracy of our model in the N_2 dominated
554 conditions.

555 Our model also suggests that the Si, O and N contents of the alloy influence the
556 siderophilicity of nitrogen. We find that Si has a negative effect on nitrogen siderophilicity (Figure
557 9a), as suggested by Grewal et al. (2019a), Shi et al. (2022), and Huang et al. (2024a). Although,
558 the magnitude of this interaction determined by Grewal et al. (2019a) is different from that
559 determined by Shi et al. (2022) and Huang et al. (2024a) likely due to differences in the assumed
560 structural form of the parameter in their models. These studies report interaction parameters that
561 do not scale with temperature, which when applied to the extreme temperatures associated with
562 core formation may underestimate the partitioning of nitrogen into the core (overpredict strength
563 of interaction).

564 Furthermore, the interaction parameter based on our model fit for N-Si interaction (ϵ_N^{Si})
565 was 9.06 (± 1.05), determined for a reference temperature of 1873 K. Our N-Si interaction

566 coefficient is fit with data that span a wide range of temperatures, and this provides confidence in
567 using the $1/T$ scaling assumed here for describing non-ideal solution terms. Application of the
568 ϵ_N^{Si} value in our model to any desired temperature considers temperature scaling of this interaction
569 term as shown in Equations 4 and 5. Considering this ϵ_N^{Si} value to compositionally recalculate the
570 KD-Si values from Figure 6a, the recalculated KD-Si values shift close to the slope predicted by
571 Fischer et al. (2015) as shown in Figure 10a.

572 Oxygen has a similar effect on nitrogen as Si, where the incorporation of oxygen into the
573 alloy makes nitrogen less siderophile (Figure 9b). Our finding is qualitatively consistent with the
574 model from Huang et al. (2024) who also report a negative effect of oxygen on nitrogen
575 siderophility. Although, the coefficient reported in their model does not scale with temperature.
576 The interaction parameter for N-O interaction in the metallic alloy (ϵ_N^O) based on our model fit was
577 $8.72 (\pm 2.68)$, determined for a reference temperature of 1873 K. Application of this term in our
578 model considers temperature scaling like ϵ_N^{Si} does above. We used this ϵ_N^O value to compositionally
579 recalculate for N-O interaction in Figure 4b. The KD-O data recalculated for N-O interaction shifts
580 up towards the model predictions from Fischer et al. (2015), despite observable differences from
581 the trend predicted by Fischer et al. (2015) (Figure 10b).

582 In contrast to the effect of Si and O, the negative self-interaction coefficient, ϵ_N^N , of 5.35
583 (± 1.56) suggests more siderophile behavior with increasing the concentration of nitrogen in metal
584 (Figure 9c). Experimental systems tend to have high nitrogen concentrations (Figure 5f), and thus
585 the N-N interaction parameter suggests current data are biased to high $D_N^{m/s}$ values when applying
586 to natural systems with low nitrogen concentrations.

587 Lastly, our model predicts that the SiO_2 content of the silicate makes nitrogen less
588 siderophile (Figure 9d). The effect of silicate melt has been quantified as NBO/T in previous
589 studies (Grewal et al., 2019a; Huang et al., 2024; Shi et al., 2022), which proxies for the structure
590 of the silicate melt. Although, the melt structure varies with pressure and temperature, as well as
591 composition (e.g. Huang et al., 2022). Nonetheless, there are discrepancies on the effect of NBO/T
592 on nitrogen siderophility. Speelmanns et al. (2019) do not observe any significant effect of the
593 NBO/T within the range of their silicate melt composition (0.1-1.3). Grewal et al. (2019a) model
594 the effect of NBO/T within a range of 0.4-2.5 and report a positive effect on nitrogen siderophility.
595 Shi et al. (2022) observe a similar effect within an NBO/T range of 0.02-3.1, suggestive of a greater
596 siderophile behavior with a more depolymerized melt. This positive correlation is also
597 corroborated by Huang et al. (2024) who explored relatively depolymerized melts with NBO/T
598 ranging between 2.4-3.2. Our experimental designs allow us to explore the effect of silicate melt
599 composition over a wide range of melt polymerization (Figure 11) with the nominal designs having
600 a range of NBO/T between 0.5- 1.1 and the MgO saturated designs between 2.7-3.7. We see a
601 similar correlation with NBO/T in our experiments as Grewal et al. (2019a), Shi et al. (2022) and
602 Huang et al. (2024), where the MgO-saturated experiments tend to witness a greater siderophile
603 behavior of nitrogen than the nominal designs (Figure 11). Though NBO/T correlates with silicate
604 melt composition as a broader term, it does not reflect the chemical interaction that nitrogen has
605 within the melt. Our model captures this chemical interaction with SiO_2 in the melt and suggests
606 that N-Si interaction in the silicate melt makes nitrogen less siderophile (Figure 9d). Although, as

607 discussed above, different silicate melt models yield similar quality of fits to the data, and we favor
608 using SiO₂ given the evidence for Si-N interactions in reduced melts (Huang et al., 2022) and the
609 relatively simple functional form. Lower SiO₂ melts are associated with more siderophile behavior
610 for N, and this is qualitatively consistent with Si-N interactions helping to stabilize N in melt.
611 Additionally, the functional form considers scaling of the symmetric regular solution parameter
612 $\omega_N^{SiO_2}$ with temperature (Eq 6), unlike NBO/T.

613 *4.4 Model Validation*

614 We used our model from Eq 7 to predict nitrogen partitioning in our multi-anvil
615 experiment. The multi-anvil experiment was run at 15 GPa and 2773 K, a PT location that has
616 relatively sparse data in the global compilation (Figure 8a) and utilizes a method that is distinct
617 from the large majority of experiments used to determine our parameterization. Predicting nitrogen
618 partitioning in this experiment, external to our global compilation, allowed us to evaluate the
619 consistency of our model beyond where there is dense PTX coverage. Our model prediction falls
620 within 95% confidence interval of the observed partition coefficient of the MA experiment (Figure
621 12). The success of our model to predict $D_N^{m/s}$ values in PTX regions with relatively poor data
622 coverage and with distinct methodology provides confidence in applying Eq 7 to natural systems.
623 Adding the MA experiment to the global compilation does not affect parameters values or identify
624 additional significant parameters.

625 *4.5 $D_N^{m/s}$ variations across PTX conditions*

626 With Eq 7 established, we can now better predict the behavior of nitrogen in an accreting
627 proto-Earth. Core formation likely proceeded from early episodes dominated by low PT conditions
628 to later episodes where more extreme PT conditions prevailed (e.g. Canup and Asphaug, 2001;
629 Tonks and Melosh, 1993). We apply our $D_N^{m/s}$ model to core formation scenarios assuming a
630 mantle liquidus from Fiquet et al. (2010) to constrain potential PT conditions of metal-silicate
631 reaction (Fig 13a). We apply the formalism in Rubie et al. (2011) to predict the major element
632 chemistry of metal and silicate reacting over the range of PT conditions considered here and apply
633 their “reduced” and an “oxidized” bulk planet compositions.

634 Predicted $D_N^{m/s}$ values for a “reduced” protoplanet are less than one (lithophile) across the
635 PT conditions we explore in Figure 13a. Low PT conditions produce a more pronounced lithophile
636 behavior of nitrogen, while $D_N^{m/s}$ values shift marginally higher as PT conditions increase. The
637 overall lithophile behavior of N throughout the PT range in Figure 13a for a reduced protoplanet
638 reflects that the net effect of the rise in Si and O with increase in temperature (forcing $D_N^{m/s}$ down)
639 remain roughly balanced by the rise in the oxygen fugacity (ΔIW) of the system and pressure
640 (forcing $D_N^{m/s}$ up) in a reduced protoplanet system.

641 Predicted $D_N^{m/s}$ values for an “oxidized” protoplanet decrease by approximately an order
642 of magnitude across the PTX range of conditions associated with these scenarios (Figure 13a).
643 Oxidizing conditions promote higher $D_N^{m/s}$ values under low PT conditions, but as PT conditions
644 increase, the effects of temperature, Si and O content work to drive down $D_N^{m/s}$ values, more than

645 offsetting the effects of pressure and oxygen fugacity. We predict little difference in $D_N^{m/s}$ values
646 above 100 GPa between oxidized and reduced protoplanets.

647 Upon applying the nitrogen partitioning model from Huang et al. (2024) to the PTX space
648 explored in Figure 13a we observe similar trends of the predicted $D_N^{m/s}$ values across both the
649 “oxidized” and the “reduced” systems (Figure 13b, c), where the siderophility of nitrogen
650 decreases with increasing PT conditions. In both scenarios, their predicted $D_N^{m/s}$ values have
651 smaller differences from our model predictions at low PT but at high PT conditions their
652 predictions suggest an order of magnitude lower siderophility of nitrogen than what our models
653 predict. Note that we assume zero C and S and an NBO/T value of 2.6 to predict $D_N^{m/s}$ using the
654 Huang et al. (2024) model.

655 *4.6 Elemental fractionations of VSEs by core formation*

656 We now apply Eq 7 towards understanding how N and other VSEs are redistributed during
657 terrestrial planet accretion. The concentration of VSEs in BSE shows a general depletion of
658 nitrogen with respect to hydrogen, sulfur and carbon when normalized to CI chondrite (Halliday,
659 2013; Hirschmann, 2016; Marty, 2012; Wasson et al., 1997). CI chondrites and the Sun are similar
660 in composition and CI chondrites may therefore provide an estimate for the VSE ratios of the bulk
661 solar system (Anders and Grevesse, 1989; Lodders, 2003; Palme et al., 2014). It is clear that many
662 processes can fractionate VSEs as witnessed by the variable VSE ratios of chondrites and varying
663 magmatic solubilities of VSE (e.g., Bergin et al., 2015; Hellmann et al., 2020; Vollstaedt et al.,
664 2020). We focus here on the ability of core formation to induce VSE fractionations on the silicate
665 portions of larger terrestrial bodies such as Earth.

666 To explore how core formation can induce VSE fractionations we first compare our
667 predicted $D_N^{m/s}$ values with the partition coefficients of other VSEs (C and S) with increasing PT
668 conditions for core-formation in an “oxidized” and a “reduced” system (Figure 13 b, c). We take
669 the exchange coefficient model of carbon from Blanchard et al. (2022) for both possible +2 and
670 +4 valence states of carbon. We also use the Eq 1 from Fischer et al. (2020) to predict $D_C^{m/s}$ which
671 includes the effects of ΔIW , light elements in the alloy (O and S) and NBO/T on carbon partitioning
672 in addition to PT terms. We assume sulfur-free calculations of $D_C^{m/s}$ when using this equation and
673 assume an NBO/T value of 2.6. The partitioning of sulfur ($D_S^{m/s}$) was calculated using Eq S-8 from
674 Jackson et al. (2021) assuming a carbon free system and the activity coefficient of Fe as one. We
675 focus on C/N and S/N ratios because carbon and sulfur are relatively well studied under higher PT
676 conditions compared to H (Blanchard et al., 2022; Dalou et al., 2017; Fischer et al., 2020; Grewal
677 et al., 2019c; Jackson et al., 2021; Tagawa et al., 2021). The predicted C and S partition coefficients
678 are plotted in Figure 13 b and c. C and S remain siderophile across the PTX space of core
679 formation, although they exhibit a lowering of this siderophile tendency with increasing PT
680 conditions. Nitrogen, in comparison, has a lower preference for the metallic alloy across the PTX
681 span regardless of the oxidation state of the system.

682 We now apply the VSE partition coefficients to a two-stage core formation model. Our
683 model is intended to model how metal-silicate reactions associated with differentiated bodies
684 impacting into a nearly fully grown Earth can fractionate VSE ratios. N-body simulations suggest

685 that this type of interaction was relatively common during the giant impact stage of planetary
 686 growth (e.g., Agnor et al., 1999; Canup and Asphaug, 2001; Wetherill, 1985). In the first stage we
 687 react metal and silicate of the impactor at 10 GPa and 2500 K for “reduced” and “oxidized”
 688 protoplanets to simulate core formation within a smaller protoplanet bodies. We calculate the
 689 composition of metal and silicate using the batch equation as follows:

$$690 \quad [i]_{metal} = \frac{D_i^{m/s} \cdot [i]_{bulk}}{D_i^{m/s} + (1 - D_i^{m/s}) \cdot f_{silicate}}$$

$$691 \quad [i]_{silicate} = \frac{[i]_{bulk}}{D_i^{m/s} + (1 - D_i^{m/s}) \cdot f_{silicate}}$$

692 Here, [i] is the N, C or S, $D_i^{m/s}$ is the partition coefficient of the element and $f_{silicate}$ is the
 693 mass fraction of the silicate phase that is in equilibrium with the reacting metal. We assume bulk
 694 1 wt % S, 1 wt % C and 100 ppm N (although only N partitioning depends on N concentration)
 695 and that the core is 1/3 of the overall protoplanet mass. Note that our model is focused on how
 696 VSE are fractionated, rather than predicting absolute concentrations, so the bulk concentrations of
 697 C and S are essentially placeholders.

698 In the second stage we then take the core from the first stage calculation and let it backreact
 699 with a deep magma ocean (100 GPa, 5000 K), also exploring “reduced” and “oxidized” protoplanet
 700 scenarios to set the VSE partition coefficients for these more extreme conditions. The goal is this
 701 step is to calculate the chemical consequences of smaller differentiated body accreting to a nearly
 702 Earth-sized differentiated body. We assume the magma ocean of the nearly Earth-sized body is
 703 devoid of VSEs before reacting with the core from the first step.

704 Figure 14a plots predicted C/N and S/N ratios of the magma ocean against the metal/silicate
 705 ratio associated with core backreaction (i.e., the second stage) for the “reduced” protoplanet
 706 scenario. VSE ratios are normalized to their bulk ratios associated with the first stage calculation.
 707 We take the metal/silicate ratio associated with backreaction as a free parameter because it depends
 708 on the fluid dynamics of the dense metal falling through the magma ocean, which are still a topic
 709 of study (Dahl and Stevenson, 2010; Deguen et al., 2014; Maas et al., 2021; Qaddah et al., 2019).
 710 At high metal/silicate ratios in Figure 14a, the predicted C/N and S/N ratios in the silicate phase
 711 are relatively low, reflecting that nitrogen is a relatively lithophile VSE near 100 GPa. As
 712 metal/silicate ratios decrease (potentially reflecting more silicate entrainment in downwelling
 713 metal-rich plumes or less emulsification of the impactor core), the C/N and S/N ratios rise and
 714 approach the composition of the impactor core from the first stage calculation (Figure 14a).

715 Figure 14b plots the predicted C/N and S/N ratios against the metal/silicate ratio associated
 716 with core backreaction within a deep magma ocean (second stage) for the “oxidized” protoplanet
 717 scenario. In this case, the impactor core from the first step calculation itself has a lower degree of
 718 VSE fractionation since nitrogen remains siderophile, although less than C and S, under low PT
 719 conditions associated with the first stage. Under deep magma ocean environments in the second
 720 step, C/N and S/N ratios in the silicate phase remain less than 1 across almost any assumed
 721 metal/silicate ratio, which is a manifestation of the oxidized impactor core having a lower C/N and

722 S/N ratio from the first stage. As the metal/silicate ratio approaches extreme metal dilution, the
723 C/N and S/N ratios in the silicate phase also approach the impactor core chemistry from the first
724 stage calculation.

725 Figure 15 illustrates core formation scenarios during the second stage calculation with
726 variable metal/silicate ratios and variable VSE fractionations. Figure 15a shows a scenario of high
727 metal/silicate ratio under which VSE fractionations would produce low C/N and S/N ratios. In
728 contrast, if the metal entrains a larger amount of the magma ocean that it reacts with (Figure 15b),
729 the magma ocean would acquire elevated C/N and S/N ratios due to the metal-silicate interaction.

730 Taken together, we find that backreaction of cores produced at lower PT conditions within
731 deep magma oceans can induce a wide variety of VSE fractionations (Figure 15). Our modeling
732 highlights the importance of redox conditions that prevailed within smaller differentiated bodies
733 and the metal/silicate ratio associated with the backreaction of impactor cores within deeper
734 (higher PT) magma oceans in modulating VSE ratios. Reduced bodies have a greater potential to
735 produce cores with elevated C/N and S/N ratios compared to oxidized bodies given the partitioning
736 of VSEs under lower PT conditions (Figure 13). The backreaction of cores from impactors within
737 deeper magma oceans offers a second opportunity to fractionate VSEs. Backreaction with a high
738 associated metal/silicate ratio imparts low C/N and S/N ratios given the relative lithophile nature
739 of N compared to other VSEs under more extreme PT conditions (Figure 13), while backreaction
740 with a low associated metal/silicate ratio imparts higher C/N and S/N ratios that approach the
741 initial ratios of the impactor cores. Bulk silicate Earth has elevated C/N and S/N ratios, and given
742 our modeling, this may point to the importance of reduced protoplanets and larger amounts of
743 silicate entrainment during later stages of core formation for setting the volatile budget of Earth.

744

745 5. Conclusion

746 Our study expands the PTX space where the partitioning behavior of nitrogen is
747 constrained, particularly for extreme PT conditions and depolymerized melts. We conducted laser-
748 heated diamond anvil cell experiments and a multi-anvil experiment, spanning pressures from 15
749 to 103 GPa and temperatures from 2573 to 5609 K, examining silicate melts with a broad range of
750 polymerization (NBO/T: 0.5-3.7). In addition to generating new PTX data, we compiled existing
751 experimental data to parameterize nitrogen partitioning between metal and silicate across a wide
752 range of PTX conditions.

753 Our model indicates that pressure, oxygen fugacity, and bulk nitrogen concentration of the
754 system make nitrogen more siderophile, while temperature, oxygen and silicon content of the
755 metallic alloy, and the SiO₂ content of the silicate melt makes nitrogen less siderophile.

756 We apply our model to explore VSE fractionations (C/N and S/N) within smaller
757 differentiated bodies as well as in larger proto-planets due to core formation. Using a two staged
758 core formation model, we find that cores of smaller (moon-Mars sized) “reduced” bodies are
759 effective candidates to impart elevated C/N and S/N ratios to the magma ocean of proto-Earth,
760 during its later stages of core formation. Finally, the amount of magma ocean that the impactor

761 core effectively interacts with during its breakdown and descent can further elevate or lower the
762 elemental ratios.

CRedit authorship contribution statement

Ekanshu Mallick: Writing- Original Draft, Writing - Review & Editing, Conceptualization, Methodology, Investigation, Data curation, Software, Validation, Formal analysis, Visualization. **Kelsey Prissel:** Investigation, Validation, Writing - Review & Editing. **Kevin Righter:** Writing - Review & Editing, Project administration. **Colin RM Jackson:** Conceptualization, Funding acquisition, Project administration, Resources, Supervision, Methodology, Investigation, Validation, Writing -Review & Editing.

Declaration of Competing Interest

The authors declare that they have no known competing financial interests or personal relationships that could have appeared to influence the work in this paper.

Acknowledgements

This project was supported by NASA Emerging Worlds Grant 80NSSC21K0377. We thank Vitali Prakapenka and Stella Chariton for support during the high-pressure experiments conducted at GeoSoilEnviroCARS (The University of Chicago, Sector 13), the Advanced Photon Source, Argonne National Laboratory, and for discussions on temperature determination using T-rax software. We thank Dongmei Cao for assistance with using the focused ion beam at Louisiana State University.

Appendix A. Supplementary materials

The following supplementary materials are included in support of this paper.

Supplementary Tables S-1, S-2, S-3

Supplementary Figures S-1, S-2, S-3, S-4

Data availability

Trax data (.spe) are available through Mendeley data at

<https://doi.org/10.17632/2r2b7p6g6m.1>

References

- Akahama, Y., Kawamura, H., 2006. Pressure calibration of diamond anvil Raman gauge to 310GPa. *Journal of Applied Physics* 100, 043516. <https://doi.org/10.1063/1.2335683>
- Albarède, F., 2009. Volatile accretion history of the terrestrial planets and dynamic implications.
- Anders, E., Grevesse, N., 1989. Abundances of the elements: Meteoritic and solar. *Geochimica et Cosmochimica Acta* 53, 197–214. [https://doi.org/10.1016/0016-7037\(89\)90286-X](https://doi.org/10.1016/0016-7037(89)90286-X)
- Badro, J., Aubert, J., Hirose, K., Nomura, R., Blanchard, I., Borensztajn, S., Siebert, J., 2018. Magnesium Partitioning Between Earth's Mantle and Core and its Potential to Drive an Early Exsolution Geodynamo. *Geophysical Research Letters* 45, 13,240–13,248. <https://doi.org/10.1029/2018GL080405>
- Badro, J., Brodholt, J.P., Piet, H., Siebert, J., Ryerson, F.J., 2015. Core formation and core composition from coupled geochemical and geophysical constraints. *Proceedings of the National Academy of Sciences* 112, 12310–12314. <https://doi.org/10.1073/pnas.1505672112>
- Bergin, E.A., Blake, G.A., Ciesla, F., Hirschmann, M.M., Li, J., 2015. Tracing the ingredients for a habitable earth from interstellar space through planet formation. *Proceedings of the National Academy of Sciences* 112, 8965–8970. <https://doi.org/10.1073/pnas.1500954112>
- Blanchard, I., Rubie, D.C., Jennings, E.S., Franchi, I.A., Zhao, X., Petitgirard, S., Miyajima, N., Jacobson, S.A., Morbidelli, A., 2022. The metal–silicate partitioning of carbon during Earth's accretion and its distribution in the early solar system. *Earth and Planetary Science Letters* 580, 117374. <https://doi.org/10.1016/j.epsl.2022.117374>
- Braukmüller, N., Wombacher, F., Funk, C., Münker, C., 2019. Earth's volatile element depletion pattern inherited from a carbonaceous chondrite-like source. *Nat. Geosci.* 12, 564–568. <https://doi.org/10.1038/s41561-019-0375-x>
- Canup, R.M., Asphaug, E., 2001. Origin of the Moon in a giant impact near the end of the Earth's formation. *Nature* 412, 708–712. <https://doi.org/10.1038/35089010>
- Dahl, T.W., Stevenson, D.J., 2010. Turbulent mixing of metal and silicate during planet accretion — And interpretation of the Hf–W chronometer. *Earth and Planetary Science Letters* 295, 177–186. <https://doi.org/10.1016/j.epsl.2010.03.038>
- Dalou, C., Füre, E., Deligny, C., Piani, L., Caumon, M.-C., Laumonier, M., Boulliung, J., Edén, M., 2019. Redox control on nitrogen isotope fractionation during planetary core formation. *Proc. Natl. Acad. Sci. U.S.A.* 116, 14485–14494. <https://doi.org/10.1073/pnas.1820719116>
- Dalou, C., Hirschmann, M.M., von der Handt, A., Mosenfelder, J., Armstrong, L.S., 2017. Nitrogen and carbon fractionation during core–mantle differentiation at shallow depth. *Earth and Planetary Science Letters* 458, 141–151. <https://doi.org/10.1016/j.epsl.2016.10.026>
- Dasgupta, R., Falksen, E., Pal, A., Sun, C., 2022. The fate of nitrogen during parent body partial melting and accretion of the inner solar system bodies at reducing conditions. *Geochimica et Cosmochimica Acta* 336, 291–307. <https://doi.org/10.1016/j.gca.2022.09.012>
- Davies, G.F., 1985. Heat deposition and retention in a solid planet growing by impacts. *Icarus* 63, 45–68. [https://doi.org/10.1016/0019-1035\(85\)90020-X](https://doi.org/10.1016/0019-1035(85)90020-X)
- Deguen, R., Landeau, M., Olson, P., 2014. Turbulent metal–silicate mixing, fragmentation, and equilibration in magma oceans. *Earth and Planetary Science Letters* 391, 274–287. <https://doi.org/10.1016/j.epsl.2014.02.007>

- Dobrosavljevic, V.V., Zhang, D., Sturhahn, W., Chariton, S., Prakapenka, V.B., Zhao, J., Toellner, T.S., Pardo, O.S., Jackson, J.M., 2023. Melting and defect transitions in FeO up to pressures of Earth's core-mantle boundary. *Nat Commun* 14, 7336. <https://doi.org/10.1038/s41467-023-43154-w>
- Elkins-Tanton, L.T., 2012. Magma Oceans in the Inner Solar System. *Annual Review of Earth and Planetary Sciences* 40, 113–139. <https://doi.org/10.1146/annurev-earth-042711-105503>
- Fiquet, G., Auzende, A.L., Siebert, J., Corgne, A., Bureau, H., Ozawa, H., Garbarino, G., 2010. Melting of Peridotite to 140 Gigapascals. *Science* 329, 1516–1518. <https://doi.org/10.1126/science.1192448>
- Fischer, R.A., Cottrell, E., Hauri, E., Lee, K.K.M., Le Voyer, M., 2020. The carbon content of Earth and its core. *Proceedings of the National Academy of Sciences* 117, 8743–8749. <https://doi.org/10.1073/pnas.1919930117>
- Fischer, R.A., Nakajima, Y., Campbell, A.J., Frost, D.J., Harries, D., Langenhorst, F., Miyajima, N., Pollok, K., Rubie, D.C., 2015. High pressure metal–silicate partitioning of Ni, Co, V, Cr, Si, and O. *Geochimica et Cosmochimica Acta* 167, 177–194. <https://doi.org/10.1016/j.gca.2015.06.026>
- Genda, H., Abe, Y., 2003. Modification of a proto-lunar disk by hydrodynamic escape of silicate vapor. *Earth Planet Sp* 55, 53–57. <https://doi.org/10.1186/BF03352462>
- Ghiorso, M.S., Carmichael, I.S.E., 1980. A regular solution model for met-aluminous silicate liquids: Applications to geothermometry, immiscibility, and the source regions of basic magmas. *Contr. Mineral. and Petrol.* 71, 323–342. <https://doi.org/10.1007/BF00374706>
- Green, D.H., Ringwood, A.E., 1963. Mineral assemblages in a model mantle composition. *Journal of Geophysical Research (1896-1977)* 68, 937–945. <https://doi.org/10.1029/JZ068i003p00937>
- Grewal, D.S., Dasgupta, R., Holmes, A.K., Costin, G., Li, Y., Tsuno, K., 2019a. The fate of nitrogen during core-mantle separation on Earth. *Geochimica et Cosmochimica Acta* 251, 87–115. <https://doi.org/10.1016/j.gca.2019.02.009>
- Grewal, D.S., Dasgupta, R., Marty, B., 2021. A very early origin of isotopically distinct nitrogen in inner Solar System protoplanets. *Nat Astron* 5, 356–364. <https://doi.org/10.1038/s41550-020-01283-y>
- Grewal, D.S., Dasgupta, R., Sun, C., Tsuno, K., Costin, G., 2019b. Delivery of carbon, nitrogen, and sulfur to the silicate Earth by a giant impact. *Sci. Adv.* 5, eaau3669. <https://doi.org/10.1126/sciadv.aau3669>
- Grewal, D.S., Dasgupta, R., Sun, C., Tsuno, K., Costin, G., 2019c. Delivery of carbon, nitrogen, and sulfur to the silicate Earth by a giant impact. *Sci. Adv.* 5, eaau3669. <https://doi.org/10.1126/sciadv.aau3669>
- Grewal, D.S., Sun, T., Aithala, S., Hough, T., Dasgupta, R., Yeung, L.Y., Schauble, E.A., 2022. Limited nitrogen isotopic fractionation during core-mantle differentiation in rocky protoplanets and planets. *Geochimica et Cosmochimica Acta* 338, 347–364. <https://doi.org/10.1016/j.gca.2022.10.025>
- Halliday, A.N., 2013. The origins of volatiles in the terrestrial planets. *Geochimica et Cosmochimica Acta* 105, 146–171. <https://doi.org/10.1016/j.gca.2012.11.015>
- Halliday, A.N., Wänke, H., Birck, J.-L., Clayton, R.N., 2001. The Accretion, Composition and Early Differentiation of Mars. *Space Science Reviews* 96, 197–230. <https://doi.org/10.1023/A:1011997206080>

- Hellmann, J.L., Hopp, T., Burkhardt, C., Kleine, T., 2020. Origin of volatile element depletion among carbonaceous chondrites. *Earth and Planetary Science Letters* 549, 116508. <https://doi.org/10.1016/j.epsl.2020.116508>
- Hirschmann, M.M., 2016. Constraints on the early delivery and fractionation of Earth's major volatiles from C/H, C/N, and C/S ratios. *American Mineralogist* 101, 540–553. <https://doi.org/10.2138/am-2016-5452>
- Holzheid, A., Sylvester, P., O'Neill, H.S.C., Rubie, D.C., Palme, H., 2000. Evidence for a late chondritic veneer in the Earth's mantle from high-pressure partitioning of palladium and platinum. *Nature* 406, 396–399. <https://doi.org/10.1038/35019050>
- Huang, D., Badro, J., 2018. Fe-Ni ideality during core formation on Earth. *American Mineralogist* 103, 1707–1710. <https://doi.org/10.2138/am-2018-6651>
- Huang, D., Brodholt, J., Sossi, P., Li, Y., Murakami, M., 2022. Nitrogen Speciation in Silicate Melts at Mantle Conditions From Ab Initio Simulations. *Geophysical Research Letters* 49, e2021GL095546. <https://doi.org/10.1029/2021GL095546>
- Huang, Dongyang, Murakami, M., Brodholt, J., McCammon, C., Petitgirard, S., 2022. Structural evolution in a pyrolitic magma ocean under mantle conditions. *Earth and Planetary Science Letters* 584, 117473. <https://doi.org/10.1016/j.epsl.2022.117473>
- Huang, D., Siebert, J., Sossi, P., Kubik, E., Avice, G., Murakami, M., 2024. Nitrogen sequestration in the core at megabar pressure and implications for terrestrial accretion. *Geochimica et Cosmochimica Acta*. <https://doi.org/10.1016/j.gca.2024.05.010>
- Jackson, C.R.M., Bennett, N.R., Du, Z., Cottrell, E., Fei, Y., 2018. Early episodes of high-pressure core formation preserved in plume mantle. *Nature* 553, 491–495. <https://doi.org/10.1038/nature25446>
- Jackson, C.R.M., Cottrell, E., Du, Z., Bennett, N.R., Fei, Y., 2021. High pressure redistribution of nitrogen and sulfur during planetary stratification. *Geochem. Persp. Let.* 37–42. <https://doi.org/10.7185/geochemlet.2122>
- Karki, B.B., Bhattarai, D., Mookherjee, M., Stixrude, L., 2010. Visualization-based analysis of structural and dynamical properties of simulated hydrous silicate melt. *Phys Chem Minerals* 37, 103–117. <https://doi.org/10.1007/s00269-009-0315-1>
- Lammer, H., Kasting, J.F., Chassefière, E., Johnson, R.E., Kulikov, Y.N., Tian, F., n.d. *Atmospheric Escape and Evolution of Terrestrial Planets and Satellites*.
- Lee, T., Papanastassiou, D.A., Wasserburg, G.J., 1976. Correction [to “Demonstration of ²⁶Mg excess in Allende and evidence for ²⁶Al”]. *Geophysical Research Letters* 3, 109–112. <https://doi.org/10.1029/GL003i002p00109>
- Li, Y., Wiedenbeck, M., Monteleone, B., Dasgupta, R., Costin, G., Gao, Z., Lu, W., 2023. Nitrogen and carbon fractionation in planetary magma oceans and origin of the superchondritic C/N ratio in the bulk silicate Earth. *Earth and Planetary Science Letters* 605, 118032. <https://doi.org/10.1016/j.epsl.2023.118032>
- Li, Y.-F., Marty, B., Shcheka, S., Zimmermann, L., Keppler, H., 2016. Nitrogen isotope fractionation during terrestrial core-mantle separation. *Geochemical Perspectives Letters* 2, 138–147. <https://doi.org/10.7185/geochemlet.1614>
- Libourel, G., Marty, B., Humbert, F., 2003. Nitrogen solubility in basaltic melt. Part I. Effect of oxygen fugacity. *Geochimica et Cosmochimica Acta* 67, 4123–4135. [https://doi.org/10.1016/S0016-7037\(03\)00259-X](https://doi.org/10.1016/S0016-7037(03)00259-X)
- Lodders, K., 2003. Solar System Abundances and Condensation Temperatures of the Elements. *ApJ* 591, 1220–1247. <https://doi.org/10.1086/375492>

- Ma, Z., 2001. Thermodynamic description for concentrated metallic solutions using interaction parameters. *Metall Mater Trans B* 32, 87–103. <https://doi.org/10.1007/s11663-001-0011-0>
- Maas, C., Manske, L., Wünnemann, K., Hansen, U., 2021. On the fate of impact-delivered metal in a terrestrial magma ocean. *Earth and Planetary Science Letters* 554, 116680. <https://doi.org/10.1016/j.epsl.2020.116680>
- Mao, H.K., Bell, P.M., Shaner, J.W., Steinberg, D.J., 2008. Specific volume measurements of Cu, Mo, Pd, and Ag and calibration of the ruby R1 fluorescence pressure gauge from 0.06 to 1 Mbar. *Journal of Applied Physics* 49, 3276–3283. <https://doi.org/10.1063/1.325277>
- Marty, B., 2012. The origins and concentrations of water, carbon, nitrogen and noble gases on Earth. *Earth and Planetary Science Letters* 313–314, 56–66. <https://doi.org/10.1016/j.epsl.2011.10.040>
- Moynier, F., Day, J.M.D., Okui, W., Yokoyama, T., Bouvier, A., Walker, R.J., Podosek, F.A., 2012. PLANETARY-SCALE STRONTIUM ISOTOPIC HETEROGENEITY AND THE AGE OF VOLATILE DEPLETION OF EARLY SOLAR SYSTEM MATERIALS. *ApJ* 758, 45. <https://doi.org/10.1088/0004-637X/758/1/45>
- Mysen, B.O., Tomita, T., Ohtani, E., Suzuki, A., 2014. Speciation of and D/H partitioning between fluids and melts in silicate-D-O-H-C-N systems determined in-situ at upper mantle temperatures, pressures, and redox conditions. *American Mineralogist* 99, 578–588. <https://doi.org/10.2138/am.2014.4575>
- O'Neill, H.St.C., Eggins, S.M., 2002. The effect of melt composition on trace element partitioning: an experimental investigation of the activity coefficients of FeO, NiO, CoO, MoO₂ and MoO₃ in silicate melts. *Chemical Geology* 186, 151–181. [https://doi.org/10.1016/S0009-2541\(01\)00414-4](https://doi.org/10.1016/S0009-2541(01)00414-4)
- Ono, S., Kikegawa, T., Hirao, N., Mibe, K., 2010. Letter. High-pressure magnetic transition in hcp-Fe. *American Mineralogist* 95, 880–883. <https://doi.org/10.2138/am.2010.3430>
- Palme, H., Lodders, K., Jones, A., 2014. Solar System Abundances of the Elements. Planets, Asteroids, Comets and The Solar System, Volume 2 of *Treatise on Geochemistry* (Second Edition). Edited by Andrew M. Davis. Elsevier, 2014., p.15-36 2. <https://doi.org/10.1016/B978-0-08-095975-7.00118-2>
- Prescher, C., Prakapenka, V.B., 2015. DIOPTAS: a program for reduction of two-dimensional X-ray diffraction data and data exploration. *High Pressure Research* 35, 223–230. <https://doi.org/10.1080/08957959.2015.1059835>
- Qaddah, B., Monteux, J., Clesi, V., Bouhifd, M.A., Le Bars, M., 2019. Dynamics and stability of an iron drop falling in a magma ocean. *Physics of the Earth and Planetary Interiors* 289, 75–89. <https://doi.org/10.1016/j.pepi.2019.02.006>
- Righter, K., Rowland II, R., Yang, S., Humayun, M., 2020. Activity coefficients of siderophile elements in Fe-Si liquids at high pressure. *Geochem. Persp. Lett.* 44–49. <https://doi.org/10.7185/geochemlet.2034>
- Roskosz, M., Bouhifd, M.A., Jephcoat, A.P., Marty, B., Mysen, B.O., 2013. Nitrogen solubility in molten metal and silicate at high pressure and temperature. *Geochimica et Cosmochimica Acta* 121, 15–28. <https://doi.org/10.1016/j.gca.2013.07.007>
- Schlichting, H.E., Sari, R., Yalinewich, A., 2015. Atmospheric mass loss during planet formation: The importance of planetesimal impacts. *Icarus* 247, 81–94. <https://doi.org/10.1016/j.icarus.2014.09.053>

- Sekiya, M., Nakazawa, K., Hayashi, C., 1980. Dissipation of the Primordial Terrestrial Atmosphere Due to Irradiation of the Solar EUV. *Progress of Theoretical Physics* 64, 1968–1985. <https://doi.org/10.1143/PTP.64.1968>
- Sha, X., Cohen, R.E., 2010. First-principles thermal equation of state and thermoelasticity of hcp Fe at high pressures. *Phys. Rev. B* 81, 094105. <https://doi.org/10.1103/PhysRevB.81.094105>
- Shen, G., Wang, Y., Dewaele, A., Wu, C., Fratanduono, D.E., Eggert, J., Klotz, S., Dziubek, K.F., Loubeyre, P., Fat'yanov, O.V., Asimow, P.D., Mashimo, T., Wentzcovitch, R.M.M., 2020. Toward an international practical pressure scale: A proposal for an IPPS ruby gauge (IPPS-Ruby2020). *High Pressure Research* 40, 299–314. <https://doi.org/10.1080/08957959.2020.1791107>
- Shi, L., Lu, W., Kagoshima, T., Sano, Y., Gao, Z., Du, Z., Liu, Y., Fei, Y., Li, Y., 2022. Nitrogen isotope evidence for Earth's heterogeneous accretion of volatiles. *Nat Commun* 13, 4769. <https://doi.org/10.1038/s41467-022-32516-5>
- Siebert, J., Badro, J., Antonangeli, D., Ryerson, F.J., 2012. Metal–silicate partitioning of Ni and Co in a deep magma ocean. *Earth and Planetary Science Letters* 321–322, 189–197. <https://doi.org/10.1016/j.epsl.2012.01.013>
- Speelmanns, I.M., Schmidt, M.W., Liebske, C., 2019. The almost lithophile character of nitrogen during core formation. *Earth and Planetary Science Letters* 510, 186–197. <https://doi.org/10.1016/j.epsl.2019.01.004>
- Tagawa, S., Sakamoto, N., Hirose, K., Yokoo, S., Hernlund, J., Ohishi, Y., Yurimoto, H., 2021. Experimental evidence for hydrogen incorporation into Earth's core. *Nat Commun* 12, 2588. <https://doi.org/10.1038/s41467-021-22035-0>
- Tonks, W.B., Melosh, H.J., 1993. Magma ocean formation due to giant impacts. *Journal of Geophysical Research: Planets* 98, 5319–5333. <https://doi.org/10.1029/92JE02726>
- Tucker, J.M., Mukhopadhyay, S., 2014. Evidence for multiple magma ocean outgassing and atmospheric loss episodes from mantle noble gases. *Earth and Planetary Science Letters* 393, 254–265. <https://doi.org/10.1016/j.epsl.2014.02.050>
- Urey, H.C., 1955. THE COSMIC ABUNDANCES OF POTASSIUM, URANIUM, AND THORIUM AND THE HEAT BALANCES OF THE EARTH, THE MOON, AND MARS* [WWW Document]. <https://doi.org/10.1073/pnas.41.3.127>
- Vollstaedt, H., Mezger, K., Alibert, Y., 2020. Carbonaceous Chondrites and the Condensation of Elements from the Solar Nebula. *ApJ* 897, 82. <https://doi.org/10.3847/1538-4357/ab97b4>
- Walker, D., Agee, C., 1989. Partitioning “equilibrium”, temperature gradients, and constraints on Earth differentiation. *Earth and Planetary Science Letters* 96, 49–60. [https://doi.org/10.1016/0012-821X\(89\)90123-4](https://doi.org/10.1016/0012-821X(89)90123-4)
- Wang, Z., Becker, H., 2013. Ratios of S, Se and Te in the silicate Earth require a volatile-rich late veneer. *Nature* 499, 328–331. <https://doi.org/10.1038/nature12285>
- Wasson, J.T., Kallemeyn, G.W., Runcorn, S.K., Turner, G., Woolfson, M.M., 1997. Compositions of chondrites. *Philosophical Transactions of the Royal Society of London. Series A, Mathematical and Physical Sciences* 325, 535–544. <https://doi.org/10.1098/rsta.1988.0066>
- Wetherill, G.W., 1985. Occurrence of Giant Impacts during the Growth of the Terrestrial Planets. *Science* 228, 877–879.
- Wu, Z., Wentzcovitch, R.M., Umemoto, K., Li, B., Hirose, K., Zheng, J.-C., 2008. Pressure-volume-temperature relations in MgO: An ultrahigh pressure-temperature scale for

Experiment	Sample Design	P (GPa)	P (GPa) ±	T (K)	T (K) ±	ΔIW	$\Delta IW \pm$	$\log D_N^{m/s}$ (at)
N28-3	MORB:FeN:MORB	38	7	2728	68	-1.91	0.03	1.026
N32-2	MORB:FeN:MORB	40	1	3395	79	-1.49	0.10	0.504
N49-1	MORB:FeN:MORB	63	2	4774	61	-1.57	0.11	0.400
N65-3	MORB:FeN:MORB	83	2	5171	60	-1.73	0.06	0.262
N39-1	MORB:FeN:MORB	52	3	4316	42	-1.87	0.01	0.404
N39-2	MORB:FeN:MORB	53	3	4845	73	-1.36	0.08	0.400
*NFO_2-2Fe-1	MORB:FeN:MORB	69	4	5038	22	-1.42	0.03	0.332
*NFO_2-2Fe-2	MORB:FeN:MORB	65	4	3434	187	-1.95	0.03	0.402
*NFO_2-4Fe-1	MORB:FeN:MORB	67	2	5120	163	-1.68	0.15	0.310
**NMO50-3	MgO:2Silicate+1FeN:MgO	68	1	5275	61	-1.24	0.06	0.608
**NMO30-2	MgO:2Silicate+1FeN:MgO	43	1	4066	420	-1.03	0.02	1.002
N75-1	MORB:FeN:MORB	86	2	5365	295	-1.42	0.04	0.277
N85-3	MORB:FeN:MORB	103	2	5609	202	-1.15	0.07	0.234
*NFO_2-1Fe-1	MORB:FeN:MORB	60	2	4937	460	-1.63	0.10	0.223
*NFO_2-1Fe-2	MORB:FeN:MORB	60	2	4868	93	-1.54	0.02	0.305
**NMO50-1	MgO:2Silicate+1FeN:MgO	67	1	4717	140	-1.05	0.02	0.788
N-MA-15-1	2MORB+1FeN	15	0.5	2773	20	-2.51	0.06	1.193

Table 1: Experimental conditions. The MORB:Fe_xN:MORB sample design represents our nominal compositional design used for the pressure series and the MgO:2Silicate+1Fe_xN:MgO design represents our MgO saturated compositional design. The N-MA-15-1 experiment is the multi-anvil experiment. Reported pressure was measured using diamond edge Raman spectroscopy and represents the average pressure in the sample chamber after heating and includes thermal pressure. Pressure uncertainties are the standard deviation of pressure measurements across the sample chamber. The temperature measurements are average values of multiple spectra collected in succession with reported uncertainties as their standard deviation. ΔIW was calculated using methods in section 3.3. Error on ΔIW was computed by propagating analytical uncertainties for FeO and Fe. $D_N^{m/s}$ is the partition coefficient of nitrogen calculated from analytical measurements in mole fraction. (*) Experiments designed with variable FeO content in starting composition to explore the effect of oxygen fugacity. (**) MgO-saturated DAC experiments.

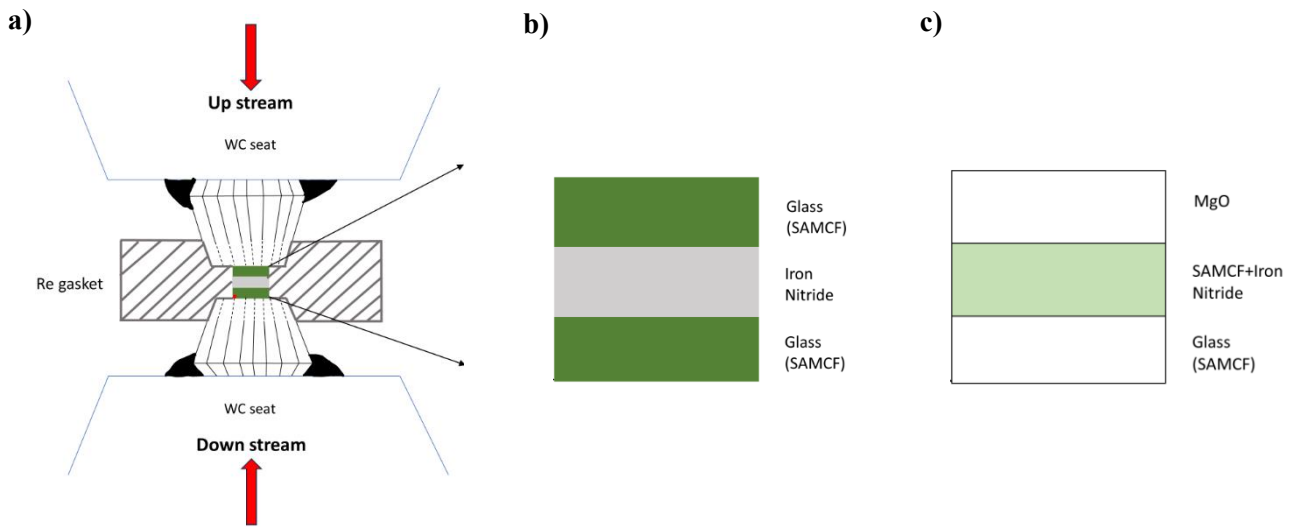


Figure 1 a) Schematic of an assembled diamond anvil cell. Red arrows: IR laser beam direction. Layered stacking of starting compositions for b) **Nominal design**, c) **MgO saturated design**. SAMCF depicts the components SiO_2 , Al_2O_3 , MgO , CaO , and FeO in the glass/silicate starting composition.

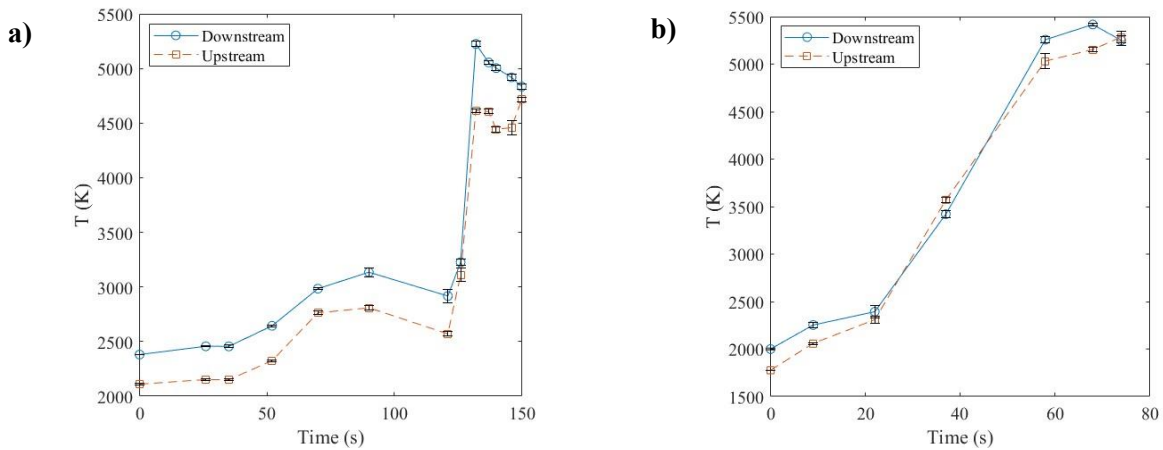


Figure 2: Time-Temperature paths of experiments a) N49-1 and b) NMO50-3. The upstream and downstream temperatures were monitored throughout the run duration of the experiment. Error bars are standard deviations on the number of T-measurements acquired at each time increment (x-axis) from the beginning of laser heating the sample marked at 0 s.

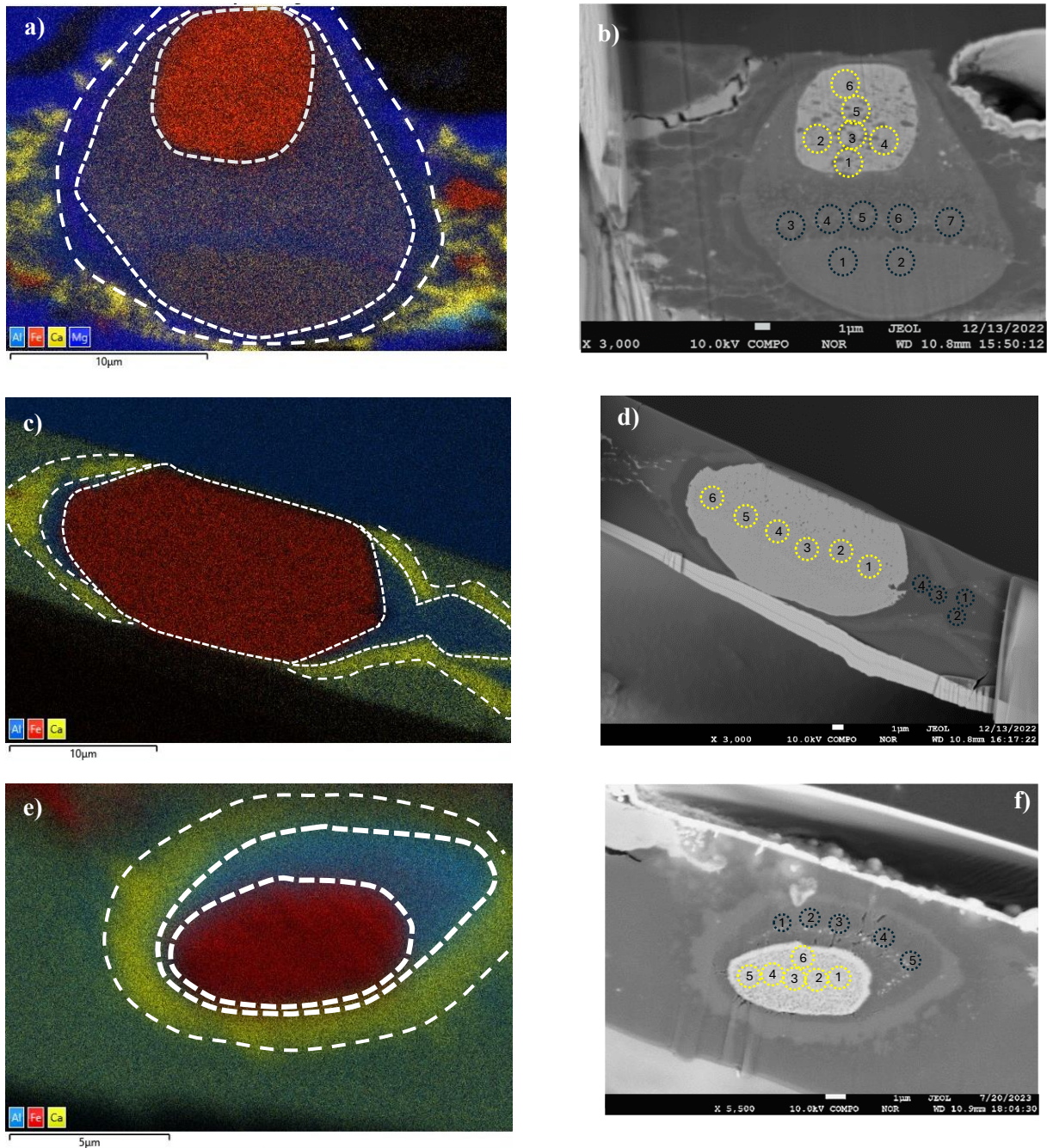


Figure 3: SE images showing cross-sections of heated spots. a) NMO50-3: [MgO-(Fe_{2.4}N+glass)-MgO] designed experiment run at 69 GPa, 5794 K showing MgSiO₃ crystallization (deep blue) around metal (red/brown)-silicate phases (light blue). **b) Compositional image for NMO50-3** c) **N49-1:[glass-Fe_{2.4}N-glass] or nominal designed experiment** run at 63 GPa, 5013 K showing CaSiO₃ crystallization (yellow) around the metal-silicate phases. **d) Compositional image for (c).** e) **N85-3: [glass-Fe_{2.4}N-glass]** run at 103 GPa, 5609 K. **f) Compositional image for (e).** Dashed blue circles are WDS measurement spots in silicate phase. Dashed yellow circles are WDS measurement spots in metallic phase. Analytical values tabulated in Table S-2 and S-3 show average values of multiple measurements on the metallic or the silicate phase as shown in these figures, along with their standard deviations, for each heated spot.

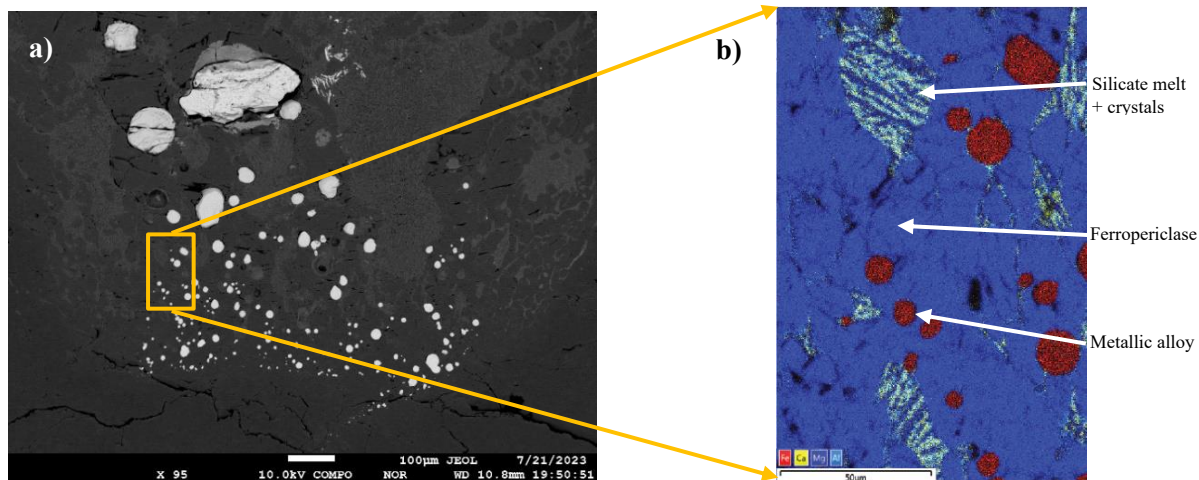


Figure 4: a) BSE image of multi-anvil experiment run at 15 GPa and 2773 K. b) zoomed in EDS map of a region within the experiment showing distribution of metallic alloy (red), silicate melt and clusters of elongated MgO, (Mg,Ca)SiO₃ crystals, and ferropericlase groundmass (blue).

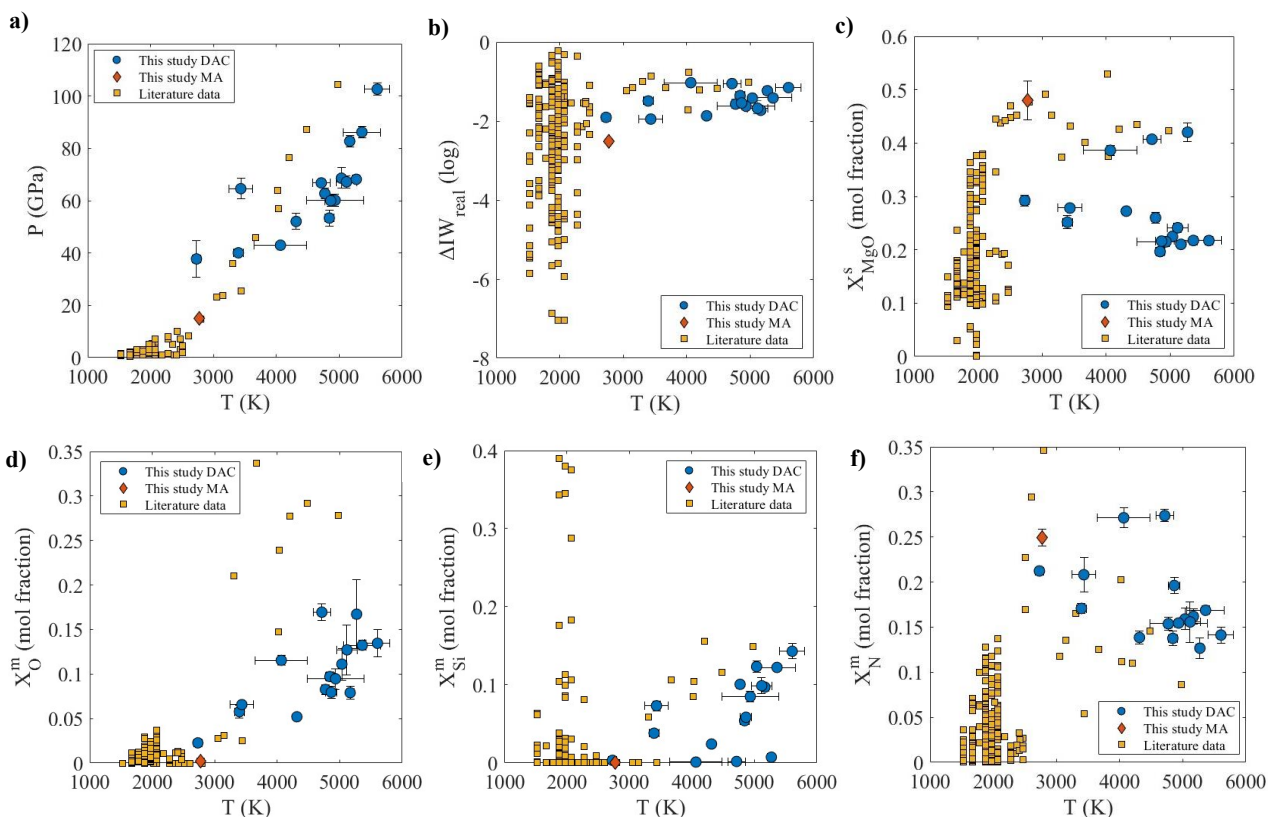


Figure 5 PTX distribution of experimental data for nitrogen partitioning between metal and silicate. a) pressure-temperature distribution, b) oxygen fugacity vs temperature distribution, c) MgO content of silicate melt (melt chemistry distribution), d) O content in the metal, e) Si content in the metal. f) N content in the metal. Error bars for our data are analytical uncertainties calculated as 1-sigma around mean.

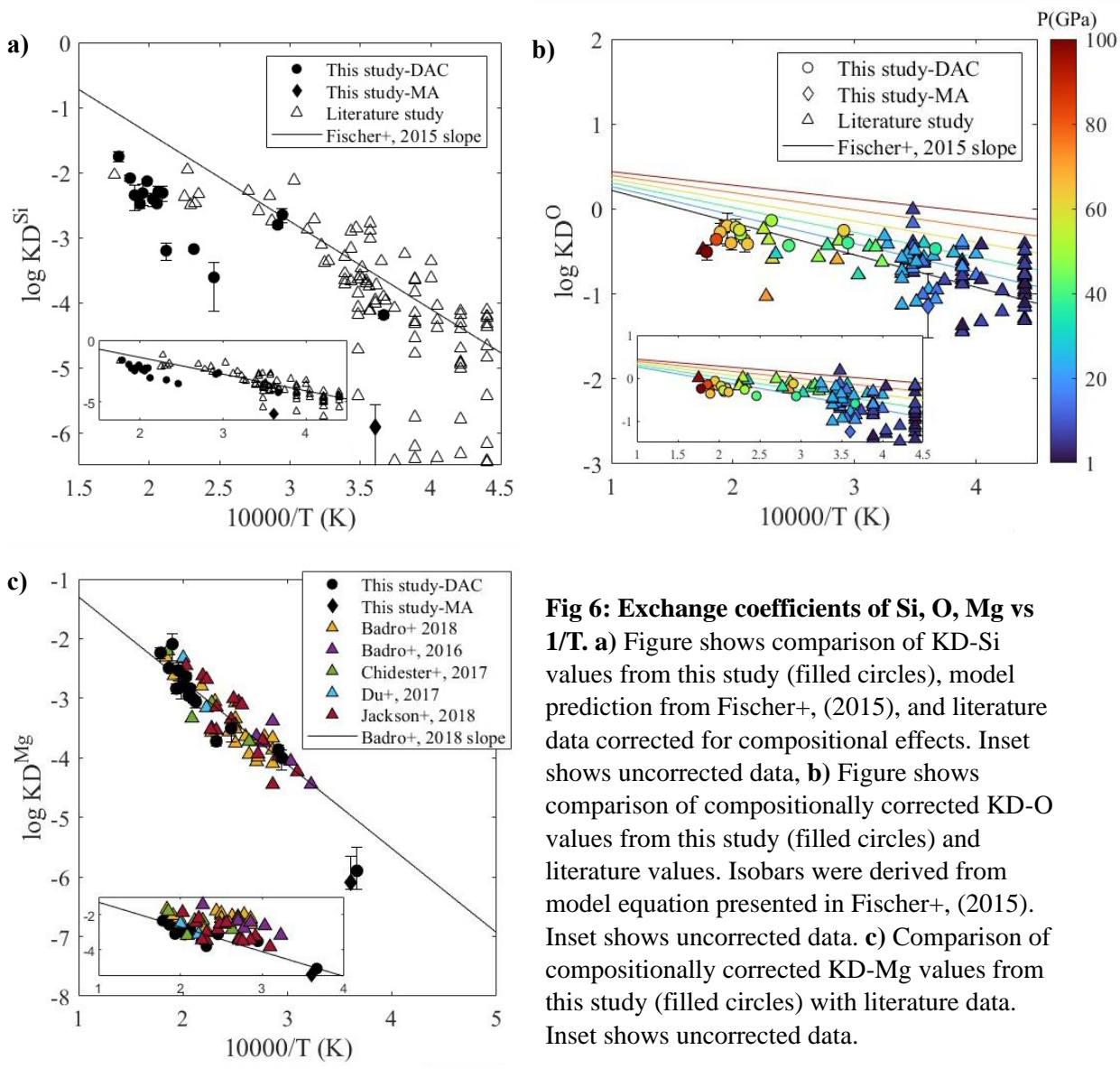


Fig 6: Exchange coefficients of Si, O, Mg vs 1/T. **a)** Figure shows comparison of KD-Si values from this study (filled circles), model prediction from Fischer+, (2015), and literature data corrected for compositional effects. Inset shows uncorrected data, **b)** Figure shows comparison of compositionally corrected KD-O values from this study (filled circles) and literature values. Isobars were derived from model equation presented in Fischer+, (2015). Inset shows uncorrected data. **c)** Comparison of compositionally corrected KD-Mg values from this study (filled circles) with literature data. Inset shows uncorrected data.

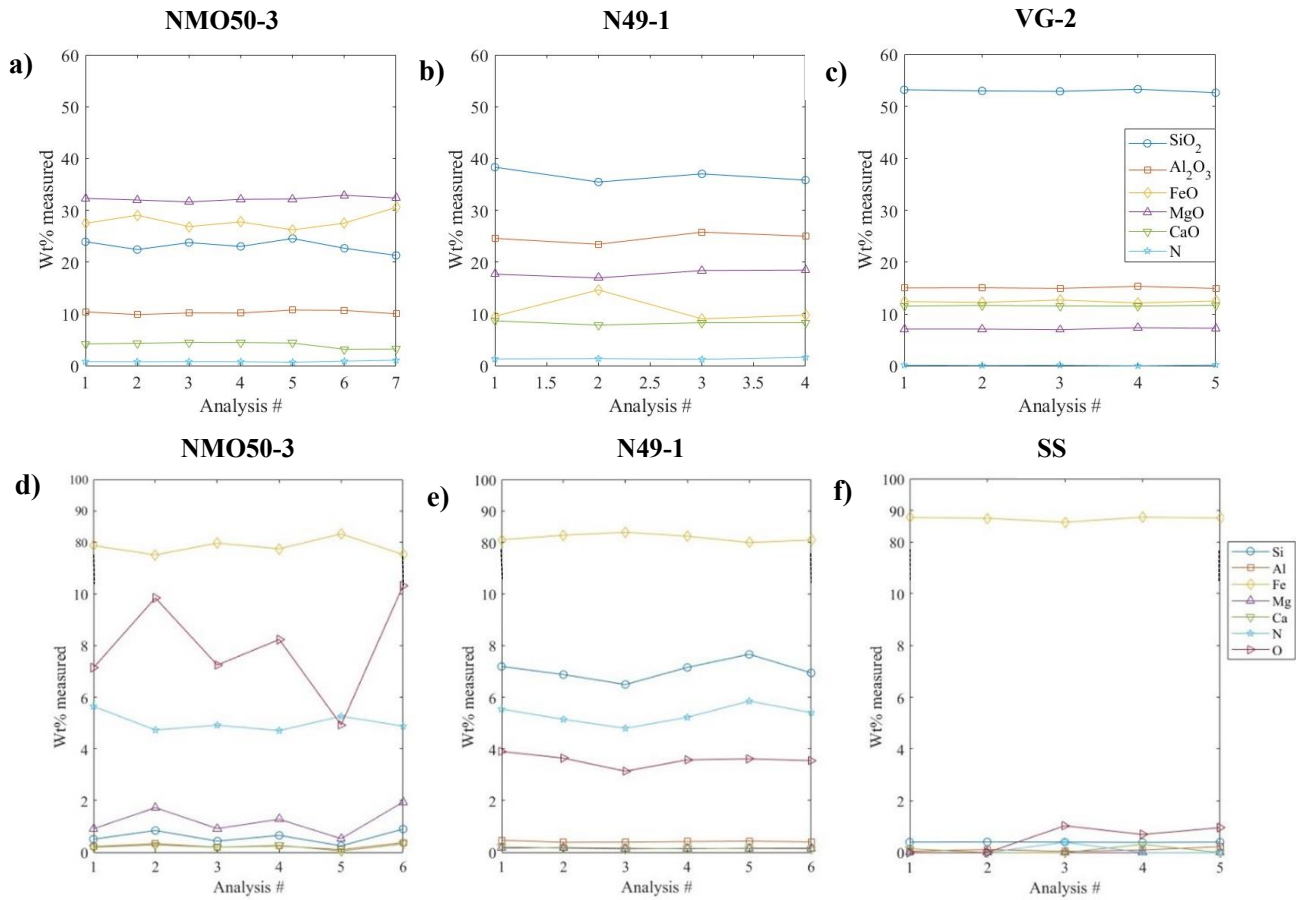


Figure 7: Microprobe (WDS) measurements across silicate a) NMO50-3, b) N49-1, c) volcanic glass (VG-2) and metallic domains d) NMO50-3, e) N49-1, f) stainless steel (SS). NMO50-3 represents the MgO saturated experiments and N49-1 represents analysis of a nominal experimental design. Analysis numbers represent individual spots within the domains in Fig 3. Volcanic glass and stainless steel are secondary standards used.

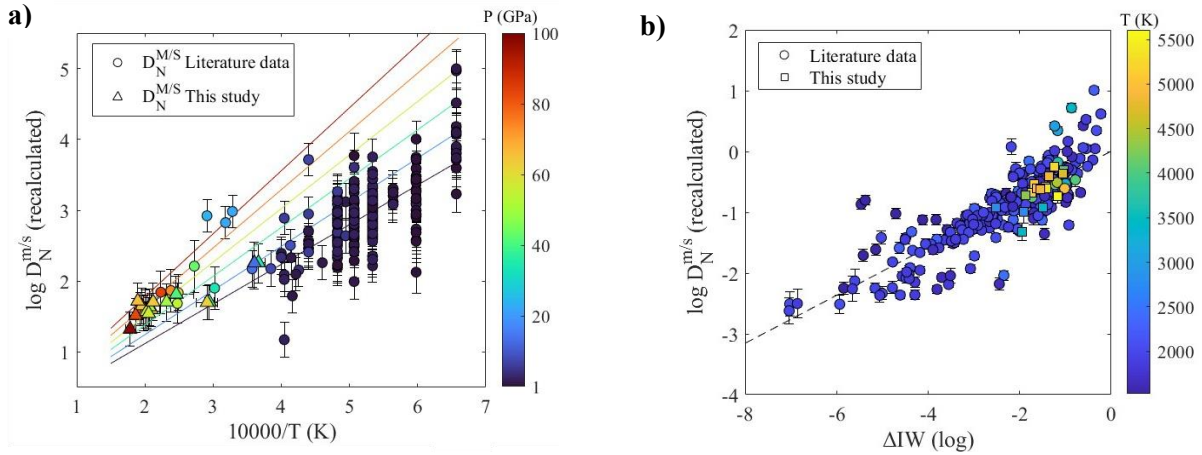


Figure 8: a) Effect of pressure and temperature on $D_N^{m/s}$. Partition coefficients are recalculated for compositional effects using our model. The isobars are our model predictions of $D_N^{m/s}$ considering the effects of pressure and temperature. Data on y-axis are recalculated to zero compositional effects and to IW. **b) Effect of oxygen fugacity on $D_N^{m/s}$.** Partition coefficients on y-axis are recalculated for the effect of P, T, and compositional effects other than oxygen fugacity using our model. Data points are color coded for the P or T they were acquired at. Error bars represent absolute uncertainties calculated from analytical uncertainties and recalculation assuming a normal distribution.

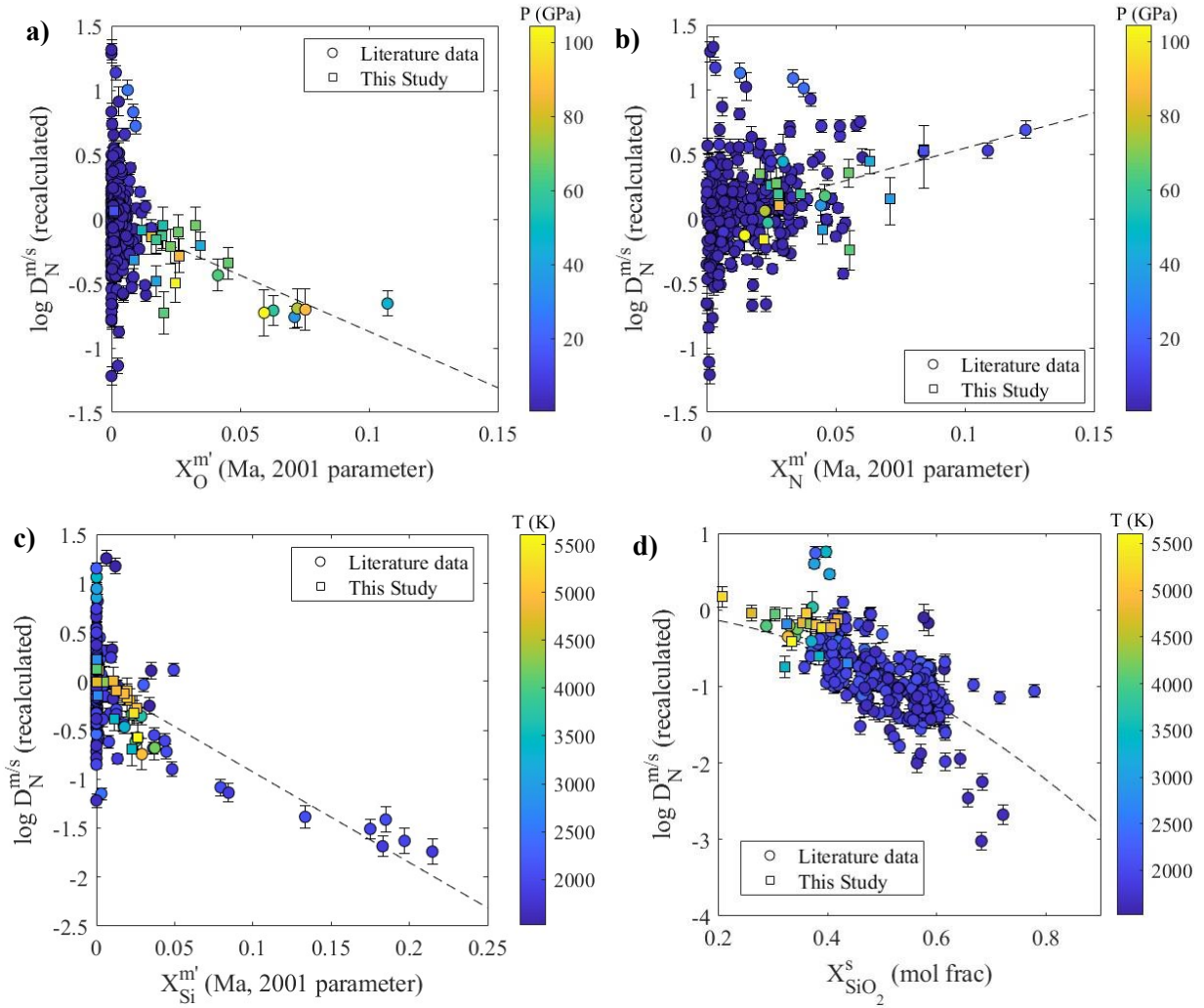


Figure 9: Effect of alloy and silicate chemistry on $D_N^{m/s}$. a) Si content and b) O content in the metallic alloy make nitrogen less siderophile. c) N enrichment in the alloy makes nitrogen more siderophile. d) SiO_2 enrichment in the silicate makes nitrogen less siderophile. X-axis represents alloy parameters of N, O and Si calculated using the Ma, (2001) approach considering the N-N, N-O and Si-N interactions. Data on y-axis are recalculated to no PTX effects and to IW except for the parameter on the respective x-axis in their functional form. Data points are color coded for the P or T they were acquired at. Error bars represent absolute uncertainties calculated from analytical uncertainties and compositional recalculation assuming a normal distribution.

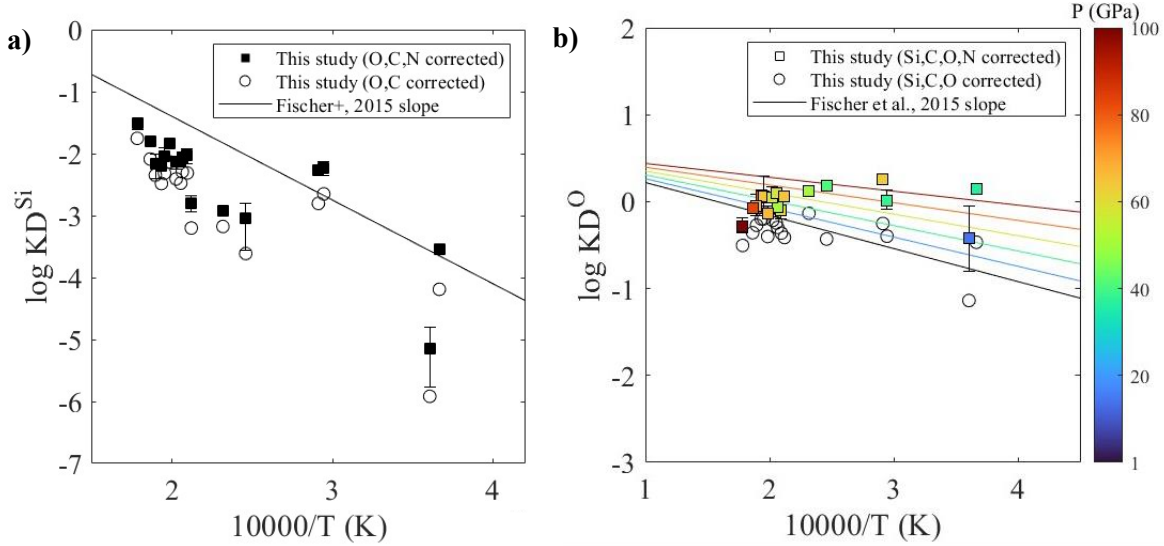


Figure 10: a) KD_{Si} recalculated for N-Si interaction. b) KD_O recalculated for N-O interaction. ϵ_N^O and ϵ_{Si}^O values were based on our model fits in Eq 7. Error bars are absolute uncertainties calculated from analytical uncertainties.

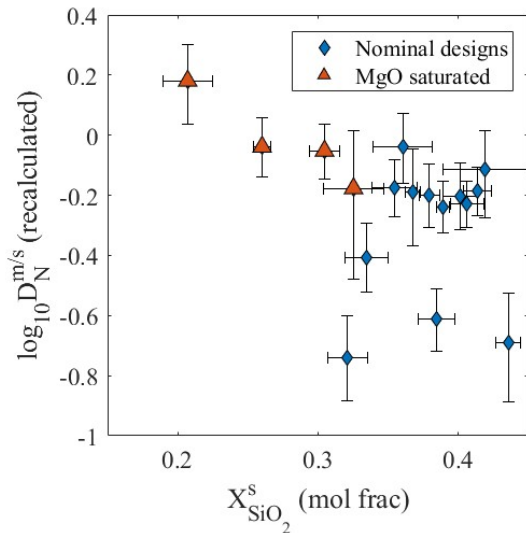


Figure 11: Effect of melt composition on D_N across different experimental designs. Partition coefficients are recalculated to IW and for no P, T, X effects except for the effect of SiO_2 . Error bars on x-axis represent analytical uncertainty. Vertical error bars are calculated by propagating analytical uncertainties through PTX recalculations based on Eq 7.

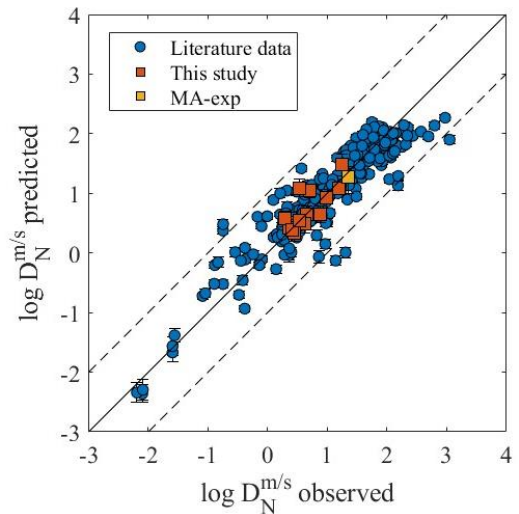


Figure 12: 1:1 comparison of Model based D_N predictions from eq 7 on y-axis with the measured (observed) $D_N^{m/s}$ values on the x-axis. The R^2 of the regression is 0.85. MA-exp is the multi-anvil data that was not included in our model formulation of Eq 7.

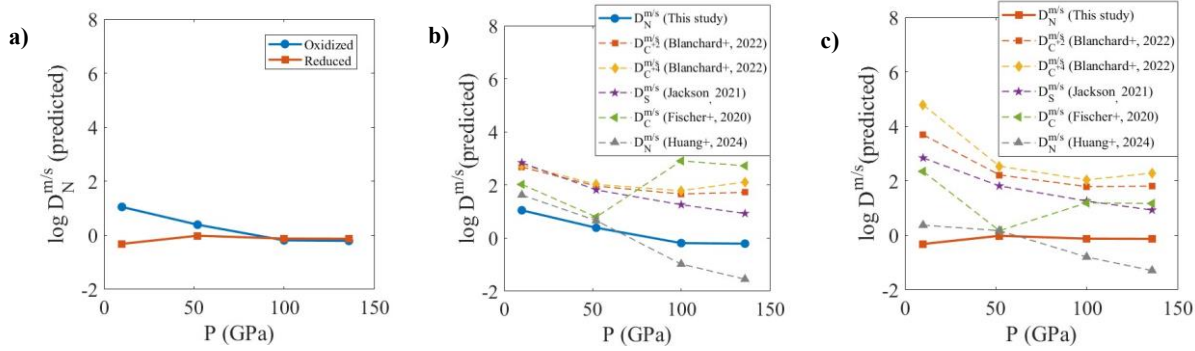


Figure 13 a) Application of nitrogen partitioning model to core formation for an oxidized system and a reduced system. Partition coefficients of N, C, H, and S across core formation PT conditions for b) oxidized protoplanet scenarios c) reduced protoplanet scenarios.

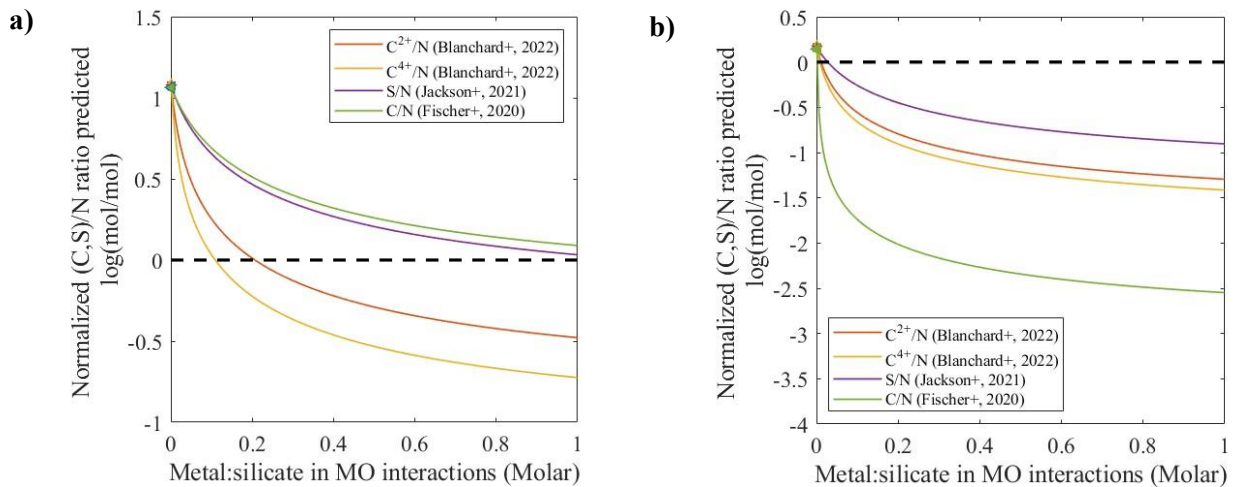


Figure 14 a) “Reduced” impact scenario, b) “Oxidized” impact scenario. C/N and S/N ratios in magma ocean (MO) environments when the smaller impactor core (equilibrated at 10 GPa, 2500 K) disintegrates and interacts with the MO under extreme PT conditions (100 GPa, 5000 K). X-axis shows the extent to which the impactor core gets diluted within the MO. Y-axis shows the S/N and the C/N ratio set in the magma ocean due to the metal-silicate interactions normalized to the bulk initial elemental ratios of the first step (see main text). Ratios above solid dashed line are elevated in C/N and S/N. Symbols at zero x-axis value are impactor core elemental ratios calculated from first step (see main text).

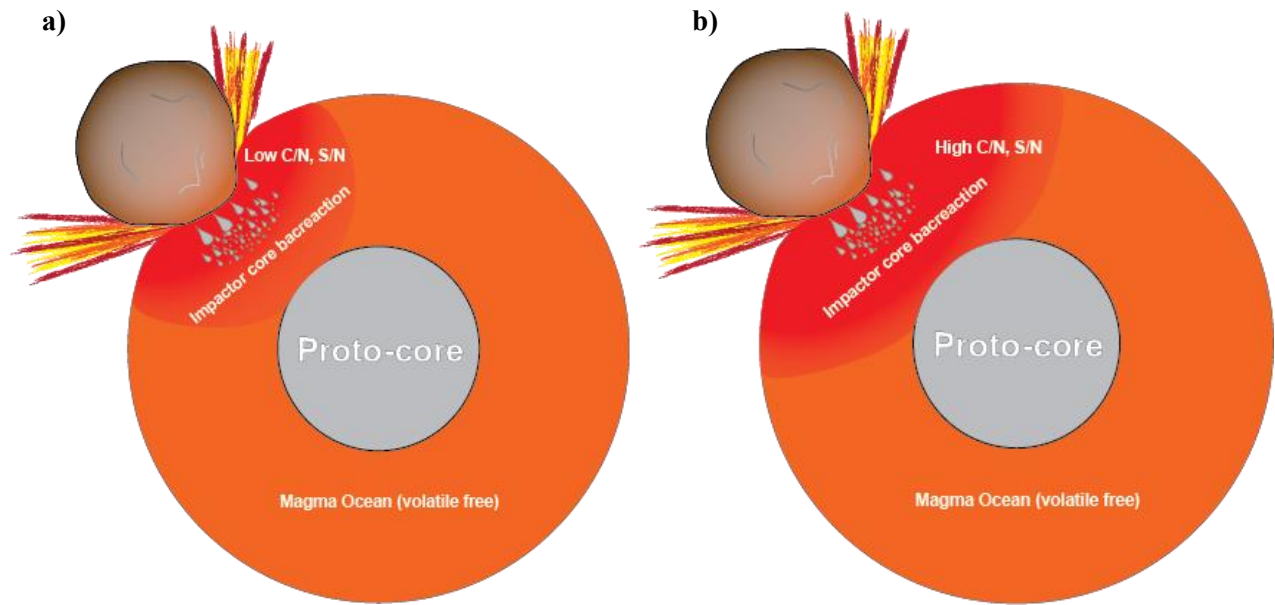


Figure 15 Schematic illustrating *second stage of core formation model*: The impactor core (gray drops) backreacts with the portion of the magma ocean it entrains (red domains within the MO). We model how VSEs are redistributed between metal and silicate, following their partitioning and the metal/silicate ratio of the reacting mass of impactor core and magma ocean. **a) shows a lower and b) shows a higher fraction of silicate mass entrained by the downwelling core of an impactor. A greater extent of metal dilution as in b) can produce elevated C/N and S/N ratios.**

Appendix A. Supplementary materials

Supplementary Tables

Table S-1: Temperature estimates for upstream (US) and downstream (DS) sides of DACs for each data point. T-rax files can be used to reproduce temperature estimates using the pixel ranges and wavelengths used to select ROI on light spectra captured on CCD.

N39-2	N28-3	N49-1	N49-2	N32-2	N75-1	N85-3	NFO_2-1Fe-1	NFO_2-1Fe-2
J8	J21	J2	J2	J9	F18	F6	F11	F11
18-36	38 to 44	1 to 13	16 to 21	21 to 36	1 to 35	54 to 78	2 to 12	13-30
35	43	13	21	35	35	77	10	29
4783	2771	4716	4342	3472	5073	5410	4467	4788
49	23	19	11	13	46	45	38	54
663-777	662-777	665-774	663-776	662-784	663-777	663-777	662-771	663-778
80-86	82-87	80-86	80-86	81-86	81-85	81-85	81-85	81-85
4907	2686	4832	4282	3318	5658	5808	5396	4951
21	72	20	123	24	20	18	16	31
660-778	662-778	661-778	661-779	661-780	662-779	661-779	660-779	672-781
130-136	131-136	131-136	131-136	131-136	130-136	131-136	130-137	131-136
4845	2728	4774	4312	3395	5365	5609	4937	4868
73	68	61	93	79	295	202	460	93

Sample name	NFO_2-4Fe-1	NFO_2-2Fe-1	NFO_2-2Fe-2	N65-3	NMO50-1	NMO50-3	NMO30-2	N39-1
Trax file name	O8	O3	O3	O17	O27	O27	O10	J8
Trax file range for hotspot (.spe)	1 to 8	11 to 19	20 to 30	21 to 26	1 to 10	21 to 30	15 to 23	1 to 16
Trax file used for temperature determination (.spe)	7	18	30	26	10	29	23	16
US (K)	4936	5022	3249	5117	4851	5300	4484	4295
± (K)	19	10	33	27	20	61	54	30
US wavelength (nm)	662-775	661-779	662-778	661-780	661-779	662-780	663-779	662-779
US pixel range	81-85	130-137	72-98	81-85	80-87	80-84	80-86	81-88
DS (K)	5282	5054	3619	5226	4579	5250	3648	4337
± (K)	17	18	19	22	25	50	30	41
DS wavelength (nm)	662-779	661-780	661-780	662-779	661-779	661-779	662-779	661-779
DS pixel range	130-135	130-137	131-136	129-135	130-136	130-135	131-135	129-136
mean T (using mid US and DS)	5120	5038	3434	5171	4717	5275	4066	4316
± (K)	163	22	187	60	140	61	420	42

Table S-2: Silicate analysis of our experimental data used for the formulation of Eq 7

NFO_2-1Fe-1	N85-3	N75-1	NMO3 0-2	NMO5 0-3	NFO_2 -4Fe-1	NFO_2 -2Fe-2	NFO_2 -2Fe-1	N39-2	N39-1	N65-3	N49-1	N32-2	N28-3
5	4	4	11	7	12	4	8	8	3	6	5	6	5
43.76	33.99	39.30	34.54	24.29	38.40	34.27	39.48	43.35	39.35	42.88	36.76	41.29	47.45
1.35	0.79	0.36	0.94	1.63	2.39	0.67	0.74	2.97	0.46	1.53	1.59	1.26	0.41
22.77	28.70	28.87	8.62	10.84	23.99	29.10	24.76	20.29	24.31	25.47	25.06	18.67	16.10
0.88	0.73	0.76	0.22	0.75	1.23	1.55	0.16	0.79	0.60	1.26	0.50	0.96	0.21
9.65	14.58	11.08	21.33	26.79	9.49	6.65	11.51	14.39	7.95	7.96	10.22	12.55	8.02
2.17	2.54	1.09	0.70	3.19	3.29	0.57	0.64	2.45	0.35	1.02	3.02	2.89	0.40
15.25	14.81	14.73	29.37	33.10	17.24	19.95	15.71	13.65	19.54	15.06	18.07	18.11	21.34
0.49	0.42	0.54	0.34	1.49	0.52	0.59	0.18	0.30	0.18	0.45	0.25	0.68	0.74
6.28	5.96	3.90	5.44	4.12	8.97	7.97	6.75	6.99	7.48	6.42	8.41	8.03	6.57
0.27	0.21	0.21	0.12	0.48	1.54	1.32	0.11	0.35	0.22	0.13	0.26	0.61	0.20
2.29	1.96	2.11	0.72	0.86	1.90	2.06	1.80	1.33	1.37	2.21	1.48	1.34	0.51
0.19	0.15	0.04	0.07	0.16	0.27	0.09	0.24	0.37	0.39	0.18	0.15	0.22	0.12
100.00	100.00	100.00	100.00	100.00	100.00	100.00	100.00	100.00	100.00	100.00	100.00	100.00	100.00

Sample name	N-MA-15-1	NMO 50-1	NFO_2-1Fe-2
n	10	6	4
SiO2	39.00	28.92	43.06
±	1.81	0.55	1.05
Al2O3	8.65	10.85	22.62
±	0.86	0.18	0.29
FeO	4.37	24.44	10.16
±	0.61	0.84	0.49
MgO	38.69	30.37	15.38
±	3.53	0.52	0.25
CaO	8.85	4.45	6.37
±	1.51	0.08	0.15
N	0.45	0.97	2.41
±	0.17	0.12	0.10
Total	100.0	100.0	100.00

* Analysis and uncertainties are in wt%.

Table S-3: Metal analysis of our experimental data used for the formulation of Eq 7

NFO_2-2Fe-2	NFO_2-2Fe-2	N39-2	N39-1	N65-3	N49-1	N32-2	N28-3
4	6	6	6	5	6	6	6
82.37	78.18	82.20	87.31	78.53	81.59	86.40	89.80
1.78	2.18	0.29	0.56	1.88	1.06	2.99	0.62
0.06	0.04	0.06	0.05	0.07	0.02	0.08	0.04
0.11	0.02	0.07	0.06	0.07	0.03	0.08	0.08
7.34	5.75	4.99	4.71	6.04	5.36	5.79	6.95
0.71	0.42	0.33	0.25	0.04	0.37	0.07	0.08
1.73	1.59	4.20	4.04	3.96	1.96	2.60	2.04
0.43	0.43	0.33	0.25	1.17	0.51	0.35	0.39
5.19	8.97	3.94	1.65	7.29	7.06	2.59	0.21
0.43	0.55	0.11	0.08	0.53	0.39	0.15	0.02
0.12	0.18	0.14	0.05	0.13	0.15	0.08	0.01
0.02	0.06	0.02	0.01	0.02	0.01	0.02	0.01
0.33	0.52	0.30	0.10	0.41	0.41	0.12	0.02
0.02	0.18	0.02	0.01	0.04	0.03	0.02	0.01
0.22	0.19	0.15	0.06	0.20	0.15	0.12	0.08
0.03	0.03	0.02	0.01	0.04	0.03	0.02	0.03
2.64	4.59	4.03	2.02	3.37	3.29	2.23	0.85
0.08	0.80	0.20	0.08	0.27	0.25	0.32	0.06
100.00	100.0	100.00	100.00	100.00	100.00	100.0	100.00

Exp Samples	N-MA-15-1	NMO 50-1	NFO_2 -1Fe-2	NFO_2 -1Fe-1	N85-3	N75-1	NMO3 0-2	NMO5 0-3	NFO_2 -4Fe-1
n	9	4	5	5	6	4	4	6	4
Fe	90.15	79.90	79.55	78.95	74.70	75.02	81.11	78.72	76.47
±	0.42	0.72	0.34	1.45	2.42	0.68	1.95	3.73	1.93
Ni	0.05	0.09	0.07	0.03	0.11	0.05	0.04	0.05	0.03
±	0.06	0.10	0.10	0.04	0.11	0.07	0.04	0.06	0.04
N	8.15	8.97	7.47	5.76	5.23	6.42	10.55	5.07	5.92
±	0.42	0.29	0.33	0.14	0.27	0.27	0.44	0.47	1.11
C	1.47	2.84	4.36	3.84	1.41	2.07	2.85	6.27	3.10
±	0.20	0.47	0.53	0.67	0.55	0.60	0.11	0.49	0.32
Si	0.01	0.14	4.48	6.37	10.65	9.35	0.08	0.59	7.58
±	0.02	0.04	0.15	0.51	0.67	0.23	0.06	0.23	1.17
Mg	0.04	0.28	0.13	0.25	0.45	0.28	0.17	1.21	0.32
±	0.04	0.05	0.01	0.01	0.07	0.02	0.07	0.49	0.08
Al	0.00	0.06	0.33	0.56	1.31	0.86	0.02	0.24	0.81
±	0.00	0.02	0.04	0.04	0.10	0.04	0.02	0.09	0.25
Ca	0.03	0.10	0.15	0.22	0.43	0.21	0.06	0.22	0.24
±	0.03	0.02	0.01	0.02	0.02	0.02	0.01	0.09	0.03
O	0.09	7.61	3.46	4.03	5.69	5.75	5.12	7.64	5.52
±	0.13	0.05	0.28	0.47	0.58	0.30	0.25	1.78	1.60
Total	100.00	100.0	100.00	100.00	100.00	100.00	100.00	100.00	100.00

* Analysis and uncertainties are in wt%.

Supplementary Figures

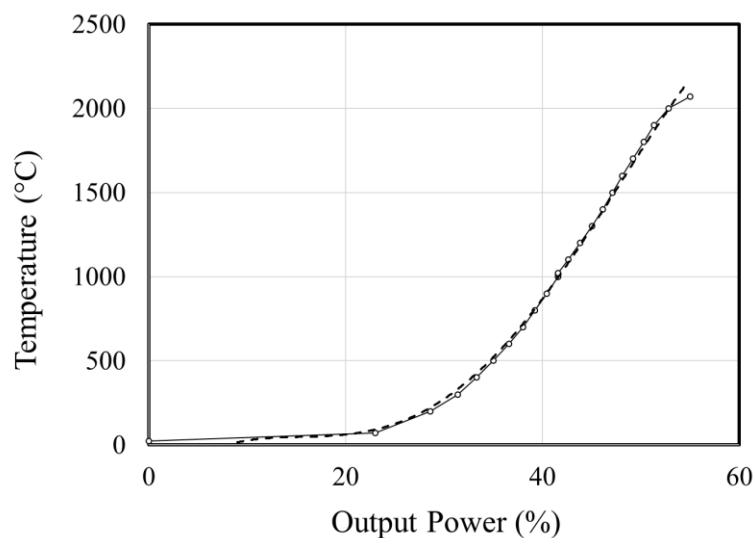


Fig S-1: Multi anvil power temperature curve. The solid curve corresponds to heating of our MA experiment. Beyond 2273 K thermocouples do not report true temperature due to contamination. Temperatures beyond 2273 K were inferred from previously run power-temperature curves (thick dashed lines)

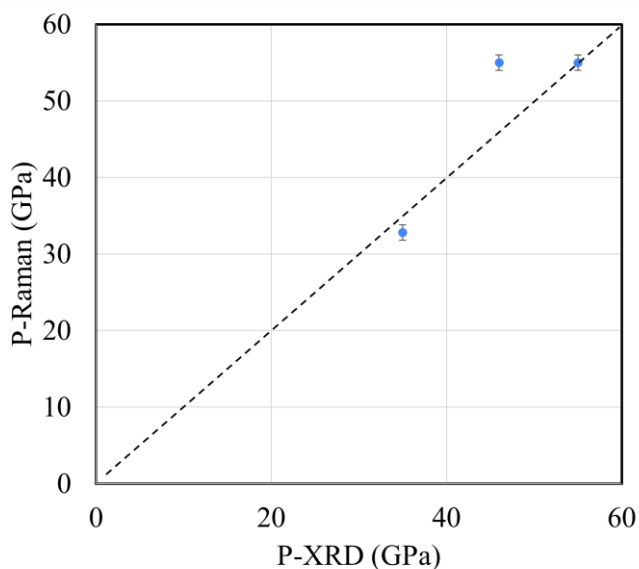


Fig S-2: Comparison of pressures measured using diamond edge Raman spectroscopy with pressures measured on the heated spots using synchrotron XRD measurements of MgO peaks. XRD based pressures estimates could be determined for MgO saturated experiments for which MgO peaks post experiments could be measured, and pressures evaluated using existing equation of states for MgO. The nominal designs did not have a pure phase for which EOS has been defined to evaluate its pressure and are not reported in this comparison. The dashed line represents a 1:1 correlation of pressures for both methods. Y-error bars are standard deviations on pressure based on Raman measurements acquired from 5 points across the sample chamber post heating.

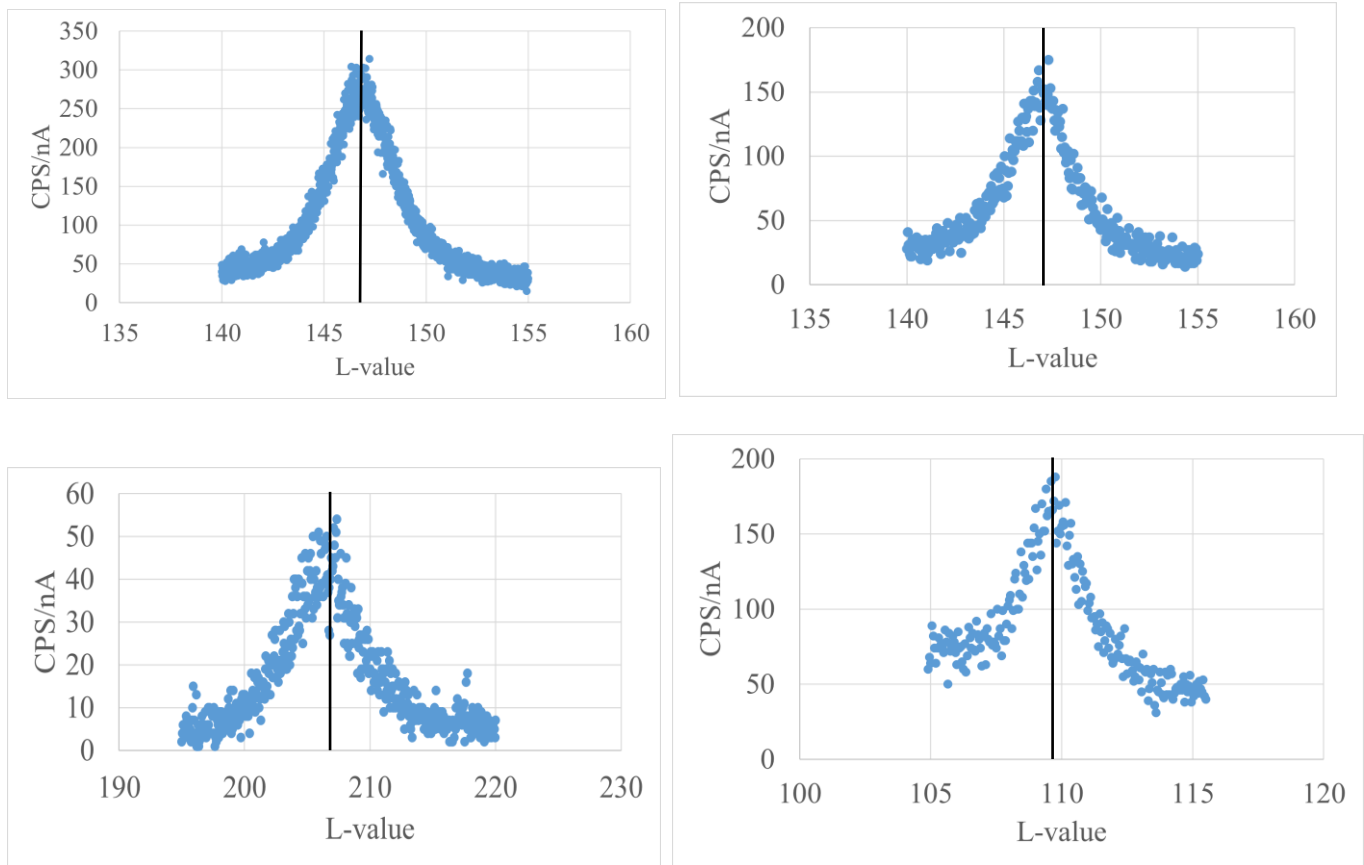


Fig S-3: Wave scans of **a) nitrogen in silicate** and **b) nitrogen c) carbon d) oxygen in metallic alloys** showing peak positions (L-value) for N, C, and O which were used to measure their concentrations. These wave scans were determined on our DAC samples. *Black solid line in the plots above denotes the peak position (x-axis) for each element.*

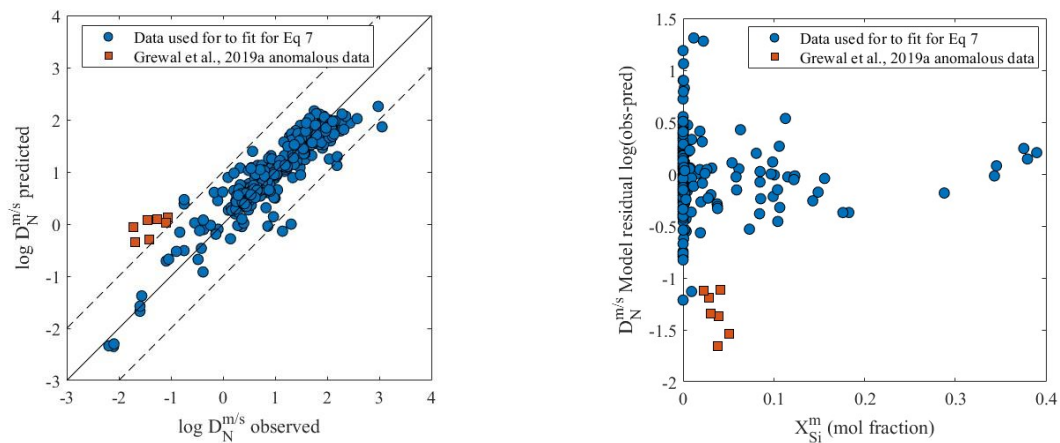


Fig S-4: **a) Comparison of predicted vs observed $D_N^{m/s}$, b) Model residual vs Si content of metal** We do not include 7 data points from Grewal et al., 2019a highlighted above. These data show systematic offset of D values from our model predictions that correlate with higher Si content in the metal. This systematic offset is not found in other Si bearing high PT and low PT experiments used in our compilation.

